Monthly Notices
of the
ROYAL ASTRONOMICAL SOCIETY

Mon. Not. R. Astron. Soc. **402,** 724–744 (2010) doi:10.1111/j.1365-2966.2009.15897.x

The spectral energy distribution of the central parsecs of the nearest AGN

M. A. Prieto,[1⋆] J. Reunanen,[2] K. R. W. Tristram,[3] N. Neumayer,[4]
J. A. Fernandez-Ontiveros,[1] M. Orienti[1] and K. Meisenheimer[5]

[1]*IAC, 38200 La Laguna, Tenerife, Spain*
[2]*Tuorla Observatory, University of Turku, Väisäläntie 20, 21500 Piikkiö, Finland*
[3]*MPIfR, Auf dem Hügel, 53121 Endenich, Bonn, Germany*
[4]*ESO, Karl-Schwarzschild-Str. 2, 85478 Garching, Germany*
[5]*MPIA, Königstuhl 17, 69117 Heidelberg, Germany*

Accepted 2009 October 23. Received 2009 October 16; in original form 2009 July 14

ABSTRACT

Spectral energy distributions (SEDs) of the central few tens of parsec region of some of the nearest, most well-studied, active galactic nuclei (AGN) are presented. These genuine AGN-core SEDs, mostly from Seyfert galaxies, are characterized by two main features: an infrared (IR) bump with the maximum in the 2–10 μm range and an increasing X-ray spectrum with frequency in the 1 to ∼200 keV region. These dominant features are common to Seyfert type 1 and 2 objects alike. In detail, type 1 AGN are clearly distinguished from type 2 by their high spatial resolution SEDs: type 2 AGN exhibit a sharp drop shortwards of 2 μm, with the optical to UV region being fully absorbed; type 1s instead show a gentle 2 μm drop ensued by a secondary, partially absorbed optical to UV emission bump. On the assumption that the bulk of optical to UV photons generated in these AGN is reprocessed by dust and re-emitted in the IR in an isotropic manner, the IR bump luminosity represents $\gtrsim$70 per cent of the total energy output in these objects, and the second energetically important contribution is the high energies above 20 keV.

Galaxies selected by their warm IR colours, i.e. presenting a relatively flat flux distribution in the 12–60 μm range, have often being classified as AGN. The results from these high spatial resolution SEDs question this criterion as a general rule. It is found that the intrinsic shape of the infrared SED of an AGN and inferred bolometric luminosity largely depart from those derived from large aperture data. AGN luminosities can be overestimated by up to two orders of magnitude if relying on IR satellite data. We find these differences to be critical for AGN luminosities below or about 10^{44} erg s^{-1}. Above this limit, AGN tend to dominate the light of their host galaxy regardless of the integration aperture size used. Although the number of objects presented in this work is small, we tentatively mark this luminosity as a threshold to identify galaxy-light-dominated versus AGN-dominated objects.

Key words: techniques: high angular resolution – galaxies: nuclei – galaxies: Seyfert – infrared: galaxies – radio continuum: galaxies – X-rays: galaxies.

1 INTRODUCTION

The study of the spectral energy distributions (SEDs) over the widest possible spectral range is an optimal way to characterize the properties of galaxies in general. Covering the widest spectral range is the key to differentiating physical phenomena, such as dust emission in the infrared (IR), stellar emission in the optical to ultraviolet (UV) and non-thermal processes in the X-rays and radio, which dominate at specific spectral ranges, and to interrelating them as most of these phenomena involve radiation reprocessing from a spectral range into another. The availability of the SED of a galaxy allows us to determine basic parameters such as its bolometric luminosity (e.g. Elvis et al. 1994; Sanders & Mirabel 1996; Vasudevan & Fabian 2007), and via modelling of the SED, its star formation level, mass and age (e.g. Bruzual & Charlot 2003; Rowan-Robinson et al. 2005; Dale et al. 2007).

The construction of bona fide SEDs is not easy as it involves data acquisition from different ranges of the electromagnetic spectrum using very different telescope infrastructure. This again introduces a further complication as the achieved spatial resolution, and with it the aperture size used, varies with the spectral range. SEDs based

⋆E-mail: aprieto@iac.es

on the integration of the overall galaxy light may be very different from those extracted from only a specific region, e.g. the nuclear region. In this specific case, the aperture size is quite important, as different light sources, such as circumnuclear star formation, the active nucleus and the subjacent galaxy light, coexist on small spatial scales and may contribute to the total nuclear output with comparable energies (e.g. Genzel et al. 1998; Reunanen, Prieto & Siebenmorgen 2009).

In the specific case of SEDs of AGN, it is often assumed that the AGN light dominates the integrated light of the galaxy at almost any spectral range and for almost any aperture. This assumption becomes mandatory at certain spectral ranges, such as the high energies, the extreme UV or the mid-to-far-IR, because of the spatial resolution limitations imposed by the available instrumentation, which currently lies in the range of several arcseconds to arcminutes at these wavelengths. In the mid- to far-IR in particular, the available data, mostly from IR satellites, are limited to spatial resolutions of a few arcseconds at best. Thus, the associated SEDs include the contribution of the host galaxy, star-forming regions, dust emission and AGN, with the first two components being measured over different spatial scales in the galaxy depending on the object distance and the spatial resolution achieved at a given IR wavelength.

In spectral ranges where high spatial resolution (HSR) is readily available, the importance, if not dominance, of circumnuclear star formation relative to that of the AGN has become clear in the UV to optical range (e.g. Munoz-Marin et al. 2007) or in the near-IR (Genzel et al. 1998). In the radio regime, the comparison of low spatial resolution and HSR maps shows the importance of the diffuse circumnuclear emission and the emission from the jet components with respect to that of the core itself (e.g. Roy et al. 1994; Elmouttie et al. 1998; Gallimore, Baum & O'Dea 2004; Lal, Shastri & Gabuzda 2004). Even with low-resolution data, a major concern shared by most works is the relevance of the host galaxy contribution to the nuclear integrated emission from the UV to optical to IR. To overcome these mixing effects introduced by poor spatial resolution, different strategies or assumptions have been followed by the community. In quasars, by their own nature, the dominance of the AGN light over the integrated galaxy light at almost any wavelength is assumed; conversely, in lower luminosity AGN, the contribution of different components is assessed via modelling of the integrated light (Edelson & Malkan 1986; Ward et al. 1987; Sanders et al. 1988; Elvis et al. 1994; Buchanan et al. 2006 among others).

In this paper, we attempt to provide a best estimate of the AGN light contribution on very nearby AGN by using very HSR data over a wide range of the electromagnetic spectrum. Accordingly, SEDs of the central few hundred parsec region of some of the nearest and brightest AGN are compiled. The work is motivated by the current possibility of obtaining subarcsec resolution data in the near-to-mid-IR of bright AGN and thus at resolutions comparable to those available with radio interferometry and the *Hubble Space Telescope* (*HST*) in the optical to UV wavelength range. This is possible, thanks to the use of adaptive optics in the near-IR, the diffraction limit resolutions provided by 8–10 m telescopes in the mid-IR as well as interferometry in the mid-IR.

The selection of targets is driven by the requirements imposed by the use of adaptive optics in the near-IR, which limits the observations to the availability of having bright point-like targets with magnitudes $V < 15$ mag in the field, and the current flux detection limits in mid-IR ground-based observations. AGN in the near Universe are sufficiently bright to satisfy these criteria. The near- to mid-IR high-resolution data used in this work come mostly from the European South Observatory (ESO) Very Large Telescope (VLT); hence this study relies on Southern targets, all well-known objects, mostly Seyfert galaxies: Centaurus A, NGC 1068, Circinus, NGC 1097, NGC 5506, NGC 7582, NGC 3783, NGC 1566 and NGC 7469. For comparison purposes, the SED of quasar 3C 273 is also included.

The compiled SEDs make use of the highest spatial resolution data available with current instrumentation across the electromagnetic spectrum. The main sources of data include VLA-A array and Australia Telescope Compact Array (ATCA) data in radio, VLT diffraction-limited images and Very Large Telescope Interferometer (VLTI) interferometry in the mid-IR, VLT adaptive-optics images in the near-infrared, and *HST* imaging and spectra in the optical–ultraviolet. Although X-rays and gamma rays do not provide such a fine resolution, information when available for these galaxies is also included in the SEDs on the assumption that above 10 keV or so, we are sampling the AGN core region. Most of the data used come from the *Chandra* and *International Gamma-Ray Astrophysics Laboratory* (*INTEGRAL*) telescopes.

The novelty in the analysis is the spatial resolutions achieved in the IR, with typical full width at half-maximum (FWHM) $\lesssim$ 0.2 arcsec in 1–5 μm and <0.5 arcsec in 11–20 μm. The availability of IR images at these spatial resolutions allows us to pinpoint the true spatial location of the AGN – which happens not to have an optical counterpart in most of the type 2 galaxies studied – and extract its luminosity within aperture diameters of a few tens of parsec. The newly compiled SEDs are presented in Section 2. Some major differences as well as similarities between the SEDs of type 1 and type 2 AGN arise at these resolutions. These are presented and discussed in Sections 3, 4 and 5. The SEDs and the inferred nuclear luminosities are further compared with those extracted in the mid-to-far-IR from large aperture data from IR satellites, and the differences are discussed in Section 6.

Throughout this paper, $H_0 = 70\,\mathrm{km\,s^{-1}\,Mpc^{-1}}$ is used. The central wavelengths of the near-IR broad-band filters used are *I* band (0.8 μm), *J* band (1.26 μm), *H* band (1.66 μm), *K* band (2.18 μm), *L* band (3.80 μm) and *M* band (4.78 μm).

2 THE HIGH SPATIAL RESOLUTION SED: DATA SOURCE

This section describes the data used in building the HSR SEDs. Each AGN is analysed in turn, and the compiled SED is shown in Fig. 1. The data used in the SEDs are listed per object in Tables 1–10. For each AGN, an upper limit to the core size determined in the near-IR with adaptive optics and/or in the mid-IR with interferometry is first provided. The data sources used in constructing the respective SEDs are described next. When found in the literature, a brief summary of the nuclear variability levels especially in the IR is provided. This is mostly to assess the robustness of the SED shape and integrated luminosities across the spectrum. Finally, as a by-product of the analysis, an estimate of the extinction in the surrounding of the nucleus based on near-IR colours derived from the HSR, mostly $J - K$, images is provided. The colour images used are shown in Fig. 2. These are relative extinction values, resulting after comparing the average colour in the immediate surrounding of the nucleus with that at further galactocentric regions, usually within the central few hundred parsecs. These reference regions are selected from areas presenting lower extinction as judged from a visual inspection of the colour images. The derived extinction does not refer to that in the line of sight of the nucleus, which could be much larger – we do not compare with the nucleus colours but with those in its surrounding.

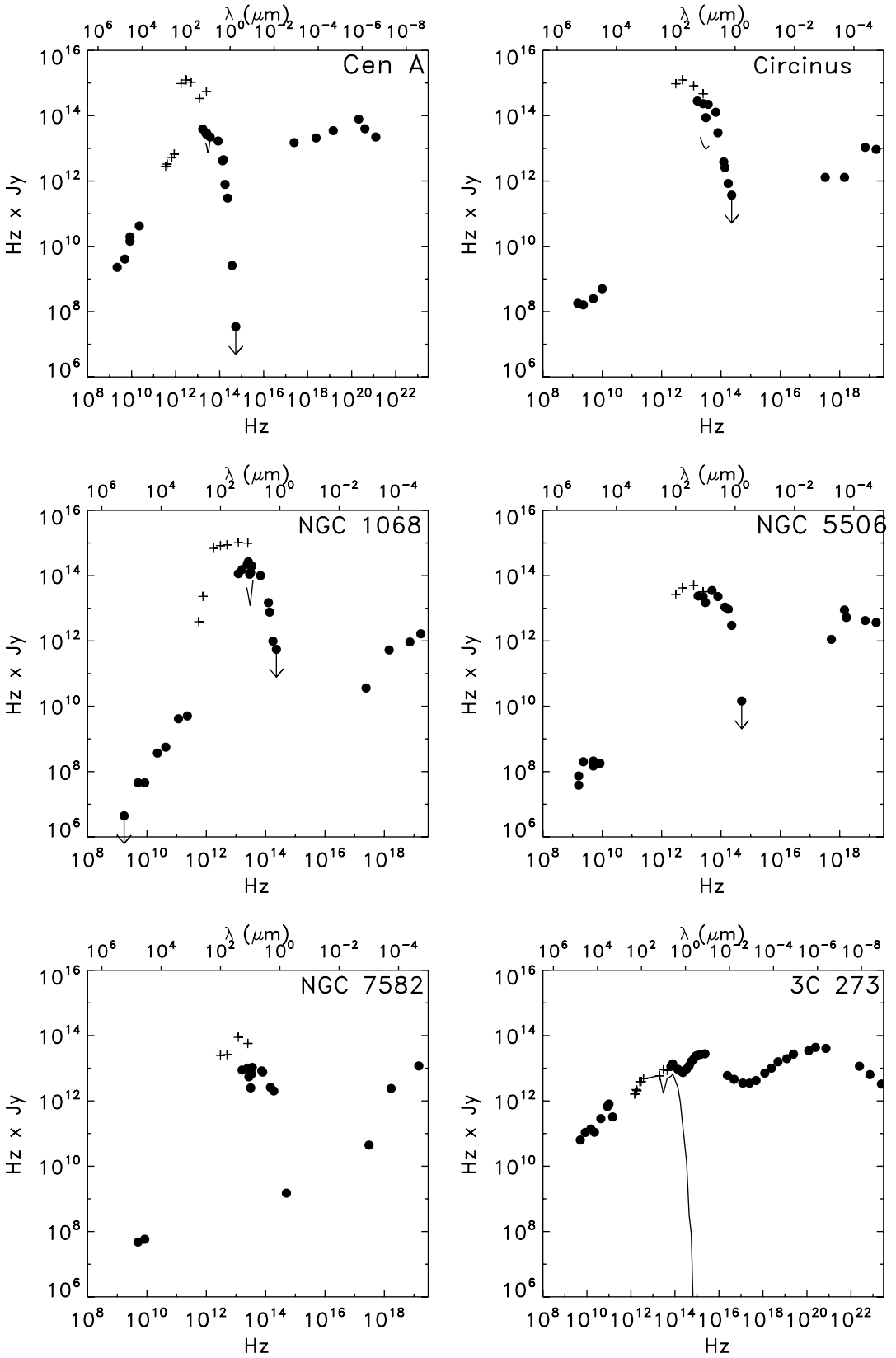

Figure 1. SEDs of the central parsec-scaled region of the AGN in this study. Filled points represent the highest spatial resolution data available for these nuclei; the thin V-shape line in the mid-IR region shown in some SEDs corresponds to the spectrum of an unresolved source as measured by VLTI/MIDI (correlated flux). Crosses refer to large aperture data in the mid-IR (mostly from *IRAS* and *ISO*) and the millimetre when available. The frequency range is the same in all plots except for Cen A and 3C 273 which extends up to the gamma rays. The continuous line in the 3C 273 plot is the SED of this object after applying an extinction $A_v = 15$ mag (see Sections 3).

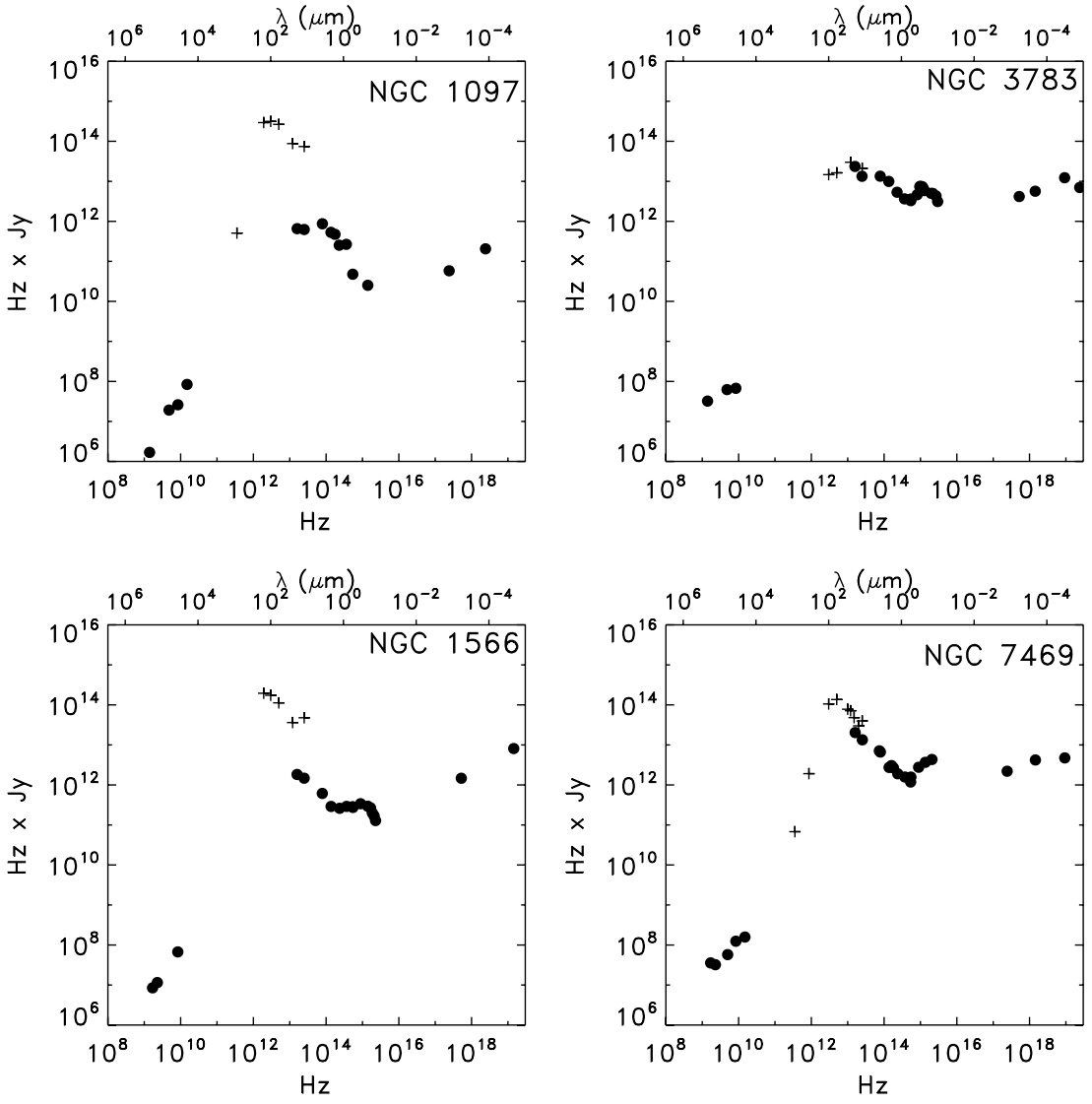

Figure 1 – *continued*

The simplest approach of considering a foreground dust screen is used. The extinction law presented in Witt, Thronson & Capuano (1992), for the UV to the near-IR, and that in Rieke & Lebofsky (1985), for the mid-IR, are used.

For some objects, the near-IR adaptive optics data used to compile the SED are presented here for the first time. For completeness purposes, Table 11 is a list of all the adaptive optics VLT/NAOS-CONICA (NACO) observations used in this work. The list of filters and dates of observations are provided. The nucleus of these AGN was in all cases bright enough to be used as a reference for the adaptive optics system to correct for the atmospheric turbulence. The optical nuclear source was used in all cases with the exception of Centaurus A and NGC 7582, for which the IR nucleus was used instead. The observation procedure and data reduction for all the objects presented here are the same as those discussed in detail in the references quoted in Table 11, we refer the interested reader to those references for further details.

There are five type 2, three type 1 and an intermediate type 1/low-ionization nuclear emission-line region (LINER) AGN in the sample, in addition to quasar 3C 273, included for comparative purposes. The AGN is unambiguously recognized in the near-IR images of all objects as the most outstanding source in the field of $26 \times 26\,\mathrm{arcsec}^2$ covered by the VLT/NACO images. This is especially the case for the type 2 sources where the AGN reveals in full realm from 2 μm longwards. The comparable resolution of the NACO-IR and the *HST*–optical images allows us to search for the optical counterpart of the IR nucleus, in some cases using accurate astrometry based on other point-like sources in the field (e.g. Prieto et al. 2004; Fernandez-Ontiveros et al. in preparation). In all the type 2 cases analysed, the counterpart optical emission is found to vanish shortwards of 1 μm. Accordingly, all the type 2 SEDs show a data gap in the optical–UV region. In addition, all the SEDs show a common data gap spanning the extreme UV-soft X-rays region, due to the observational inaccessibility of this spectral range, and the mid-IR to millimetre range, due to the lack of data at subarcsec resolution scales. Surprisingly, for some of these well-studied objects, neither radio data at subarcsec scales exist, e.g. Circinus galaxy. In these cases, we still include the available arcsec resolution radio data in the SED.

The SEDs are further complemented with available data in the X-rays, which extend up to 100–200 keV for all sources. Only for

Table 1. SED of the Centaurus A core region.

Origin	Hz	Jy
COMPTEL 5.1 MeV	1.25×10^{21}	1.78×10^{-8}
COMPTEL 1.7 MeV	3.98×10^{20}	1.0×10^{-7}
COMPTEL 0.86 MeV	2.09×10^{20}	3.75×10^{-7}
INTEGRAL 20–100 keV	1.45×10^{19}	2.4×10^{-6}
INTEGRAL 2–10 keV	2.42×10^{18}	8.8×10^{-6}
Chandra 1 keV	2.42×10^{17}	6.2×10^{-5}
WFPC2-F555W	5.40×10^{14}	$<6.4 \times 10^{-8}$
WFPC2-F814W	3.68×10^{14}	7.0×10^{-6}
NACO-*J*	2.30×10^{14}	0.0013
NACO-*H*	1.76×10^{14}	0.0045
NACO-2.02 μm	1.48×10^{14}	0.030
NACO-*K*	1.36×10^{14}	0.031
NACO-*L*	8.57×10^{13}	0.20
MIDI-8 μm	3.70×10^{13}	0.60
MIDI-12 μm	2.50×10^{13}	1.1
MIDI-13 μm	2.30×10^{13}	1.3
MIDIcorre-8.3 μm	3.60×10^{13}	0.47
MIDIcorre-9.3 μm	3.20×10^{13}	0.28
MIDIcorre-10.4 μm	2.88×10^{13}	0.25
MIDIcorre-11.4 μm	2.63×10^{13}	0.43
MIDIcorre-12.6 μm	2.30×10^{13}	0.62
VISIR-11.88 μm	2.56×10^{13}	1.1
VISIR-18.72 μm	1.70×10^{13}	2.3
VLBA-1997	2.22×10^{10}	1.9
VLBA-1997	8.40×10^{9}	1.7
VLBA-1999	8.4×10^{9}	2.32
VLBA-1999	5.0×10^{9}	0.83
VLBA-1999	2.2×10^{9}	1.03
==========		
IRAS-12 μm	2.50×10^{13}	22.0
IRAS-25 μm	1.20×10^{13}	28.0
IRAS-60 μm	5.00×10^{12}	2.1×10^{2}
IRAS-100 μm	3.00×10^{12}	4.1×10^{2}
ISO-170 μm	1.76×10^{12}	5.4×10^{2}
SCUBA-350 μm	8.66×10^{11}	7.7
SCUBA-450 μm	6.67×10^{11}	7.9
SCUBA-750 μm	4.07×10^{11}	8.1
SCUBA-850 μm	3.50×10^{11}	8.1

Note. Data sources and associated spatial resolutions are given in Section 2.1. The large aperture data in the IR, shown with crosses in the SED in Fig. 1, are added at the end of the table.

Table 2. SED of the Circinus core region.

Origin	Hz	Jy
INTEGRAL 40–100 keV	1.69×10^{19}	5.5×10^{-7}
INTEGRAL 20–40 keV	7.25×10^{18}	1.5×10^{-6}
INTEGRAL 2–10 keV	1.45×10^{18}	8.9×10^{-7}
ROSAT 1.3 keV	3.25×10^{17}	4.0×10^{-6}
NACO-*J*	2.30×10^{14}	<0.0016
NACO-*H*	1.76×10^{14}	0.0048
NACO-*K*	1.36×10^{14}	0.019
NACO-2.42 μm	1.24×10^{14}	0.031
NACO-*L*	7.90×10^{13}	0.38
NACO-*M*	6.70×10^{13}	1.9
MIDIcorr-8 μm	4.00×10^{13}	0.30
MIDIcorr-9.6 μm	3.10×10^{13}	0.30
MIDIcorr-11 μm	2.50×10^{13}	0.50
MIDIcorr-12 μm	2.00×10^{13}	1.1
MIDI-8 μm	3.70×10^{13}	6.0
MIDI-9.6 μm	3.10×10^{13}	2.8
VISIR-11.88 μm	2.50×10^{13}	9.3
VISIR-18.72 μm	1.60×10^{13}	17.6
ATCA-3 cm	1.00×10^{10}	0.050
ATCA-6 cm	5.00×10^{9}	0.050
ATCA-13 cm	2.30×10^{9}	0.070
ATCA-20 cm	1.50×10^{9}	0.12
==========		
IRAS-12 μm	2.50×10^{13}	19.0
IRAS-25 μm	1.20×10^{13}	68.0
IRAS-60 μm	5.00×10^{12}	249
IRAS-100 μm	3.00×10^{12}	316

Note. Data sources and associated spatial resolutions are given in Section 2.2. The large aperture data in the IR, shown with crosses in the SED in Fig. 1, are added at the end of the table.

Cen A and 3C 273, the SEDs are further extended to the gamma rays, these being the only two so far detected at these high energies.

2.1 Centaurus A

Centaurus A is the nearest radio galaxy in the Southern hemisphere. The adopted scale is 1 arcsec $\sim$ 16 pc ($D = 3.4$ Mpc; Ferrarese et al. 2007). The nucleus of this galaxy begins to show up in the optical longwards of 0.7 μm (Marconi et al. 2000) and so far remains unresolved down to a size of $\ll$1 pc FWHM in the 1–10 μm range (from VLT adaptive optics near-IR imaging by Haering-Neumayer et al. 2006 and VLT interferometry in the mid-IR by Meisenheimer et al. 2007).

The currently compiled SED of Cen A core is shown in Fig. 1 (Table 1). The radio data are from Very Long Baseline Array (VLBA) quasi-simultaneous observations collected in 1997 at 22.2 and 8.4 GHz (March epoch was selected) and in 1999 at 8.4, 5 and 2.2 GHz, in all cases with resolution of a few milliarcsec (Tingay & Murphy 2001; Tingay, Preston & Jauncey 2001). These spatial resolutions allow for a better separation of the core emission from the jet. The peak values reported by the authors are included in the SED.

In the millimetre range, peak values from Submillimeter Common-User Bolometric Array (SCUBA) in the 350–850 μm range from Leeuw et al. (2002) are included in the SED. SCUBA has poor spatial resolution, FWHM $\sim$ 10–15 arcsec; however, we take these measurements as genuine core fluxes as they follow fairly well the trend defined by the higher resolution data at both radio and mid-IR wavelengths. This common trend is a strong indication that the AGN is the dominant light source in the millimetre range.

In the mid-IR range, VLT/VLT Spectrometer and Imager for the Mid-Infrared (VISIR) diffraction-limited data, taken on 2006 March, at 11.9 and 18.7 μm, from Reunanen et al. (2009) are included in the SED. Further mid-IR data are from VLTI/Mid-Infrared Interferometric Instrument (MIDI) interferometric observations in the 8–12 μm range taken on 2005 February and May with resolutions of 30 mas (Meisenheimer et al. 2007). The visibility's analysis indicates that at least 60 per cent of the emission detected by MIDI come from an unresolved nucleus with a size of FWHM <1 pc at 10 μm. This is also confirmed by more recent MIDI observations by Burtscher et al. (in preparation). The SED includes two sets of MIDI fluxes measured directly in the average spectrum from both periods: (1) the total integrated flux in the MIDI aperture (0.52×0.62 arcsec^2) and (2) the core fluxes measured on the correlated spectrum. At 11.9 μm, the MIDI total flux and the VISIR nuclear flux, both from comparable aperture sizes, differ by 15 per cent.

Table 3. SED of the NGC 1068 core region.

Origin	Hz	Jy
INTEGRAL 40–100 keV	1.69×10^{19}	9.8×10^{-8}
INTEGRAL 20–40 keV	7.25×10^{18}	1.3×10^{-7}
EXOSAT 2–10 keV	1.45×10^{18}	3.7×10^{-7}
Chandra 1 keV	2.42×10^{17}	1.5×10^{-7}
NACO-*J*	2.30×10^{14}	<0.0024
NACO-*H*	1.76×10^{14}	0.0056
NACO-*K*	1.36×10^{14}	0.056
NACO-2.42 μm	1.24×10^{14}	0.12
NACO-*M*	6.70×10^{13}	1.5
MIDIcorr-8 μm	3.75×10^{13}	1.9
MIDIcorr-9.6 μm	3.1×10^{13}	0.4
MIDIcorr-12 μm	2.5×10^{13}	1.2
MIDIcorr-13 μm	2.3×10^{13}	1.9
Subaru-8.72 μm	3.4×10^{13}	5.81
Subaru-9.69 μm	3.1×10^{13}	4.03
Subaru-10.38 μm	2.9×10^{13}	3.82
Subaru-11.66 μm	2.6×10^{13}	10.2
Subaru-12.33 μm	2.4×10^{13}	9.3
Subaru-18.5 μm	1.60×10^{13}	9.6
Keck-25 μm	1.20×10^{13}	9.6
IRAM-1 mm	2.30×10^{11}	0.022
IRAM-3 mm	1.15×10^{11}	0.036
VLA-A	4.30×10^{10}	0.013
VLA-A	2.25×10^{10}	0.016
VLBA	8.40×10^{9}	0.0054
VLBA	5.00×10^{9}	0.0091
VLBA	1.70×10^{9}	<0.0026
==========		
IRAS-12 μm	2.50×10^{13}	40.0
IRAS-25 μm	1.20×10^{13}	85.0
IRAS-60 μm	5.00×10^{12}	1.8×10^{2}
IRAS-100 μm	3.00×10^{12}	2.8×10^{2}
ISO-170 μm	1.76×10^{12}	3.9×10^{2}
MKO-390 μm	7.69×10^{11}	30.0
CTIO-540 μm	5.55×10^{11}	7.0

Notes. Data sources and spatial scales are given in Section 2.3. The large aperture data in the IR, shown with crosses in the SED in Fig. 1, are added at the end of the table.

The difference is still compatible with the photometry errors which in particular may be large in the MIDI spectrum photometry.

The near-IR is covered with VLT/ NACO adaptive optics data taken in *J*-, *H*, *K* and *L* bands and in the narrow-band line-free filter centred at 2.02 μm. These are complemented with *HST*/Wide Field Planetary Camera 2 (WFPC2) data in the *I* band (Marconi et al. 2000). Shortwards of this wavelength, Cen A's nucleus is unseen. An upper limit derived from the *HST*/WFPC2 image at 0.5 μm is included in the SED.

At high energies, Cen A's nucleus becomes visible again, as well as its jet. The SED includes the 1 keV nuclear flux extracted by Evans et al. (2004) from *Chandra* observations in 2001 and average of the 100 keV fluxes derived by Rothschild et al. (2006) from *INTEGRAL* observations collected in 2003–2004. In the gamma rays, the SED includes *Imaging Compton Telescope (COMPTEL)* measurements in the 1–30 MeV range taken during the 1991–1995 campaign by Steinle et al. (1998).

For comparative purposes, Fig. 1 includes large aperture data – identified with crosses – in the mid-to-far-IR region selected from *Infrared Space Observatory* (*ISO*; Stickel et al. 2004,) and *Infrared Astronomical Satellite* (*IRAS*; Sanders et al. 2003). For consistency

Table 4. SED of the NGC 1097 core region.

Origin	Hz	Jy
ASCA 2–10 keV	2.42×10^{18}	8.5×10^{-8}
ASCA 0.5–4 keV	2.42×10^{17}	2.4×10^{-7}
WFPC2-F218W	1.40×10^{15}	1.8×10^{-5}
WFPC-F555W	5.41×10^{14}	8.8×10^{-5}
ACSWF-F814W	3.60×10^{14}	0.000 74
NACO-*J*	2.30×10^{14}	0.0011
NACO-*H*	1.76×10^{14}	0.0027
NACO-*K*	1.36×10^{14}	0.0039
NACO-*L*	7.90×10^{13}	0.011
VISIR-11.88 μm	2.50×10^{13}	0.025
VISIR-18.72 μm	1.60×10^{13}	0.041
VLA-B	1.50×10^{10}	0.0056
VLA-A	8.40×10^{9}	0.0031
VLA-A	4.80×10^{9}	0.004
VLA-B	1.40×10^{9}	0.0012
==========		
IRAS-12 μm	2.50×10^{13}	3.0
IRAS-25 μm	1.20×10^{13}	7.3
IRAS-60 μm	5.00×10^{12}	53.0
IRAS-100 μm	3.00×10^{12}	1.0×10^{2}
Spitzer-160 μm	1.92×10^{12}	1.5×10^{2}
SCUBA-850 μm	3.53×10^{11}	1.4

Notes. Data sources and spatial scales are given in Section 2.4. The large aperture data in the IR, shown with crosses in the SED in Fig. 1, are added at the end of the table.

Table 5. SED of the NGC 5506 core region.

Origin	Hz	Jy
INTEGRAL 40–100 keV	1.69×10^{19}	2.2×10^{-7}
INTEGRAL 20–40 keV	7.25×10^{18}	5.8×10^{-7}
INTEGRAL 2–10 keV	1.45×10^{18}	6.1×10^{-6}
Einstein 0.2–4 keV	5.25×10^{17}	2.1×10^{-6}
WFPC2-*V*+*R*	5.00×10^{14}	$<2.9 \times 10^{-5}$
NACO-*J*	2.30×10^{14}	0.013
NACO-*H*	1.76×10^{14}	0.053
NACO-*K*	1.36×10^{14}	0.080
NACO-*L*	7.90×10^{13}	0.29
ISO-spec-6 μm	5.00×10^{13}	0.70
TIMMI2-spec-9.6 μm	3.0×10^{13}	0.5
VISIR-11.88 μm	2.50×10^{13}	0.9
VISIR-18.72 μm	1.70×10^{13}	1.4
VLBA-1997	8.33×10^{9}	0.022
VLBI-1994	5.00×10^{9}	0.034
VLBA-1997	5.00×10^{9}	0.030
VLBA-2000	5.00×10^{9}	0.042
PTI-1990	2.30×10^{9}	0.087
VLBA-1997	1.60×10^{9}	0.024
VLBA-2000	1.60×10^{9}	0.046
==========		
IRAS-12 μm	2.50×10^{13}	1.3
IRAS-25 μm	1.20×10^{13}	4.2
IRAS-60 μm	5.00×10^{12}	8.4
IRAS-100 μm	3.00×10^{12}	8.9

Note. Data sources and corresponding spatial scales are given in Section 2.5. The large aperture data in the IR, shown with crosses in the SED in Fig. 1, are added at the end of the table.

Table 6. SED of the NGC 7582 core region.

Origin	Hz	Jy
SAX 20–100 keV	1.45×10^{19}	8.1×10^{-7}
XMM 2–12 keV	1.69×10^{18}	1.4×10^{-6}
ASCA 0.5-2- keV	3.03×10^{17}	1.46×10^{-7}
WFPC2-F606W	5.00×10^{14}	3.0×10^{-6}
NICMOS-F160W	1.88×10^{14}	0.011
NACO-2.06 μm	1.46×10^{14}	0.018
NACO-*L*	7.89×10^{13}	0.096
NACO-4.05 μm	7.41×10^{13}	0.11
TIMMI2-spec-8.5 μm	3.53×10^{13}	0.3
TIMMI2-spec-9 μm	3.33×10^{13}	0.2
TIMMI2-spec-9.6 μm	3.13×10^{13}	0.08
TIMMI2-spec-11 μm	2.73×10^{13}	0.2
TIMMI2-spec-12 μm	2.50×10^{13}	0.4
VISIR-11.88 μm	2.52×10^{13}	0.40
VISIR-18.72 μm	1.60×10^{13}	0.55
VLA-A	8.40×10^{9}	0.0069
VLA-A	5.00×10^{9}	0.0095
==========		
IRAS-12 μm	2.50×10^{13}	2.3
IRAS-25 μm	1.20×10^{13}	7.4
IRAS-60 μm	5.00×10^{12}	5.2
IRAS-100 μm	3.00×10^{12}	8.3

Note. Data sources and spatial scales are given in Section 2.6. The large aperture data in the IR, shown with crosses in the SED in Fig. 1, are added at the end of the table.

Table 7. SED of the NGC 1566 core region.

Origin	Hz	Jy
SAX 20–100 keV	1.45×10^{19}	5.6×10^{-7}
Einstein 2–4 keV	5.25×10^{17}	2.8×10^{-6}
FOS-1300 A	2.30×10^{15}	5.6×10^{-5}
FOS-1400 A	2.10×10^{15}	8.0×10^{-5}
FOS-1800 A	1.67×10^{15}	0.000 16
FOS-2100 A	1.40×10^{15}	0.000 21
WFPC2-160BW	1.87×10^{15}	0.000 11
WFPC2-F336W	8.92×10^{14}	0.000 38
WFPC2-F547M	5.48×10^{14}	0.000 50
WFPC2-F555W	5.40×10^{14}	0.000 53
WFPC2-F814W	3.68×10^{14}	0.000 79
NACO-*J*	2.37×10^{14}	0.0011
NACO-*K*	1.38×10^{14}	0.0021
NACO-*L*	7.90×10^{13}	0.0078
VISIR-11.88 μm	2.50×10^{13}	0.059
VISIR-18.72 μm	1.60×10^{13}	0.11
ATCA-8.4 GHz	8.40×10^{9}	0.0080
PTI-2.3 GHz	2.30×10^{9}	0.0050
PTI-1.7 GHz	1.70×10^{9}	<0.006
==========		
IRAS-12 μm	2.50×10^{13}	1.9
IRAS-25 μm	1.20×10^{13}	3.0
IRAS-60 μm	5.00×10^{12}	22.0
IRAS-100 μm	3.00×10^{12}	58.0
Spitzer-160 μm	1.92×10^{12}	1.0×10^{2}

Note. Data sources and spatial scales are given in Section 2.7. The large aperture data in the IR, shown with crosses in the SED in Fig. 1, are added at the end of the table.

Table 8. SED of the NGC 3783 core region.

Origin	Hz	Jy
OSSE 50–150 keV	2.42×10^{19}	2.9×10^{-7}
INTEGRAL 17–60 keV	9.31×10^{18}	1.3×10^{-6}
XMM 2–10 keV	1.45×10^{18}	3.9×10^{-6}
Einstein 0.2–4 keV	5.25×10^{17}	7.9×10^{-6}
FUSE-1040 A	3.00×10^{15}	0.001
STIS-1150 A	2.70×10^{15}	0.0016
STIS-1346 A	2.20×10^{15}	0.0023
STIS-1480 A	2.00×10^{15}	0.0025
STIS-2279 A	1.30×10^{15}	0.0045
STIS-2419 A	1.20×10^{15}	0.0056
STIS-2640 A	1.13×10^{15}	0.0065
STIS-2900 A	1.00×10^{15}	0.0075
STIS-3100 A	9.70×10^{14}	0.0076
LCO-U	8.19×10^{14}	0.0056
ACS-F547M	5.48×10^{14}	0.0060
ACS-F550M	5.45×10^{14}	0.0066
WFPC2-F814W	3.68×10^{14}	0.0099
NACO-*J*	2.30×10^{14}	0.023
NACO-*K*	1.36×10^{14}	0.073
NACO-*L*	7.90×10^{13}	0.17
VISIR-11.88 μm	2.50×10^{13}	0.54
VISIR-18.72 μm	1.60×10^{13}	1.47
VLA-A	8.40×10^{9}	0.0080
VLA-A	4.80×10^{9}	0.013
VLA-A	1.40×10^{9}	0.023
==========		
IRAS-12 μm	2.50×10^{13}	0.84
IRAS-25 μm	1.20×10^{13}	2.5
IRAS-60 μm	5.00×10^{12}	3.3
IRAS-100 μm	3.00×10^{12}	4.9

Note. Data sources and corresponding spatial scales are given in Section 2.8. The large aperture data in the IR, shown with crosses in the SED in Fig. 1, are added at the end of the table.

purposes, given the poor spatial resolution of the SCUBA data, these are also labelled with crosses in the SED.

Cen A is a strongly variable source at high energies, where flux variations could be up to an order of magnitude (Bond et al. 1996). However, during the *COMPTEL* observations used in the SED the observed variability on the scales of few days is reported to be at the 2σ level at most (Steinle et al. 1998). Combining the Oriented Scintillation Spectrometer Experiment (OSSE), *COMPTEL* and Energetic Gamma Ray Experiment Telescope (EGRET), the gamma-ray luminosity (50 keV–1 GeV) varies by 40 per cent. No report on variability monitoring of this source in the IR was found. The comparison between the VLT/VISIR data used in this work and equivalent mid-IR data obtained 4 yr apart, 2002, by Whysong & Antonucci (2004) using Keck and Siebenmorgen, Krugel & Spoon (2004) using ESO/Thermal Infrared Multimode Instrument (TIMMI2), indicates a difference with VISIR in the 40–50 per cent range. Cen A's nucleus is the single source in this study whose HSR SED, from radio to millimetre to IR, can be fitted with a single synchrotron model (Prieto et al. 2007; see also end of Section 6.3). Thus, a flux difference of a factor of 2 in the IR is consistent with genuine nuclear variability and the dominance of a non-thermal component in the IR spectral region of this nucleus.

Relative extinction values in the nuclear region of Cen A were measured from VLT/NACO $J - K$ (Fig. 2) and $H - K$ colour maps. The average reddest colours around the nucleus are $J - K \sim 1.5$ and $J - H \sim 1.5$, and the bluest colours within ~100 pc distance

Table 9. SED of the NGC 7469 core region.

Origin	Hz	Jy
INTEGRAL 17–60 keV	9.31×10^{18}	5.1×10^{-7}
XMM 2–10 keV	1.45×10^{18}	2.9×10^{-6}
ROSAT 0.1–2.4 keV	2.42×10^{17}	9.1×10^{-6}
WFPC2-F218W	1.36×10^{15}	0.0027
ACS-F330W	8.92×10^{14}	0.0031
WFPC2-F547M	5.47×10^{14}	0.0029
ACS-F550M	5.38×10^{14}	0.0022
ACS-F814W	3.75×10^{14}	0.0042
NACO-*J*	2.37×10^{14}	0.0080
NACO-*H*	1.81×10^{14}	0.015
NICMOS-F187N	1.60×10^{14}	0.019
NACO-*K*	1.38×10^{14}	0.020
NACO-*L*	7.89×10^{13}	0.084
NACO-4.05 μm	7.41×10^{13}	0.096
VISIR-11.88 μm	2.53×10^{13}	0.53
VISIR-18.72 μm	1.60×10^{13}	1.27
VLA-A	1.49×10^{10}	0.011
VLA-A	8.40×10^{9}	0.015
MERLIN	5.00×10^{9}	0.012
VLBI	2.30×10^{9}	0.014
VLBI	1.70×10^{9}	0.021
==========		
IRAS-12 μm	2.50×10^{13}	1.6
Spitzer-15 μm	2.00×10^{13}	1.5
Spitzer-20 μm	1.50×10^{13}	3.2
IRAS-25 μm	1.20×10^{13}	6.0
Spitzer-30 μm	9.99×10^{12}	7.8
IRAS-60 μm	5.00×10^{12}	27.3
IRAS-100 μm	3.00×10^{12}	35.2
Caltech-350 μm	8.57×10^{11}	2.23
SCUBA-850 μm	3.53×10^{11}	0.19

Note. Data sources and spatial scales are given in Section 2.9. The large aperture data in the IR, shown with crosses in the SED in Fig. 1, are added at the end of the table.

Table 10. SED of the 3C 273 core region.

Origin	Hz	Jy
1 GeV	2.42×10^{23}	1.4×10^{-11}
300 MeV	7.25×10^{22}	8.8×10^{-11}
100 MeV	2.42×10^{22}	4.8×10^{-10}
3 MeV	7.25×10^{20}	5.6×10^{-8}
1 MeV	2.40×10^{20}	1.8×10^{-7}
500 keV	1.21×10^{20}	2.9×10^{-7}
100 keV	2.42×10^{19}	1.1×10^{-6}
50 keV	1.21×10^{19}	1.6×10^{-6}
20 keV	4.84×10^{18}	3.3×10^{-6}
10 keV	2.42×10^{18}	4.2×10^{-6}
5 keV	1.21×10^{18}	5.9×10^{-6}
2 keV	4.84×10^{17}	8.7×10^{-6}
1 keV	2.42×10^{17}	1.4×10^{-5}
0.5 keV	1.21×10^{17}	2.9×10^{-5}
0.2 keV	4.84×10^{16}	9.5×10^{-5}
0.1 keV	2.42×10^{16}	2.48×10^{-4}
1300 A	2.31×10^{15}	0.012
2100 A	1.43×10^{15}	0.019
3000 A	9.99×10^{14}	0.025
U	8.57×10^{14}	0.027
B	7.00×10^{14}	0.027
V	5.50×10^{14}	0.029
R	4.43×10^{14}	0.027
I	3.37×10^{14}	0.028
NACO-*J*	2.30×10^{14}	0.032
NACO-*H*	1.76×10^{14}	0.047
NACO-*K*	1.36×10^{14}	0.068
NACO-*L*	7.90×10^{13}	0.17
NACO-*M*	6.70×10^{13}	0.17
VLBI-2 mm	1.47×10^{11}	2.2
VLBI-3 mm	1.00×10^{11}	8.0
VLBI	8.60×10^{10}	7.88
VLBI	4.30×10^{10}	6.66
VLBI	2.20×10^{10}	4.99
VLBA	1.50×10^{10}	9.18
VLBI	5.00×10^{9}	12.7
==========		
ISO-6.7 μm	4.44×10^{13}	0.19
ISO-14.3 μm	2.00×10^{13}	0.29
ISO-80 μm	3.70×10^{12}	1.29
ISO-100 μm	2.90×10^{12}	1.35
ISO-120 μm	2.52×10^{12}	1.55
ISO-150 μm	1.86×10^{12}	1.11
ISO-170 μm	1.72×10^{12}	1.29
ISO-180 μm	1.62×10^{12}	1.06
ISO-200 μm	1.47×10^{12}	1.09

Note. The SED from 1 GeV to the *I* band is taken directly from Turler et al. (1999). Further data are compiled in this work and the sources are given in Section 3 for this object. The large aperture data in the IR, shown with crosses in the SED in Fig. 1, are added at the end of the table.

from the nucleus are $J - K = 0.68$ and $J - H = 1.04$. Taking these as reference colours for the Cen A stellar population, the inferred extinction around the nucleus is $A_V \sim 5$–7 mag. By comparison, the extinction inferred from the depth of the silicate 9.6 μm feature in the line of sight of the nucleus – from the VLT/MIDI-correlated spectra – is a factor 2–3 larger, $A_v \sim 13$–19 mag (see Table 12).

2.2 Circinus

Circinus is the second closest AGN in the Southern hemisphere. The adopted scale is 1 arcsec $\sim$ 19 pc ($D = 4.2$ Mpc; Freeman et al. 1977). Circinus's nucleus is the only one in our sample that is spatially resolved in the VLT/ NACO adaptive optics images from 2 μm onwards. The nucleus resolves into an elongated, $\sim$2 pc size, structure oriented perpendicular to the ionization-gas cone axis (Prieto et al. 2004). Its SED is compatible with dust emission at a characteristic temperature of 300 K; this structure has thus most of the characteristics of the putative nuclear torus (Prieto et al. 2004). Further VLTI/MIDI interferometry in the 8–12 μm range also resolves the central emission into a structure of the same characteristics (Tristram et al. 2007).

Circinus's SED is shown in Fig. 1 (Table 2). The highest spatial resolution radio data available for this source – in the range of a few arcsecs only – are presented by Elmouttie et al. (1998). Because of this poor resolution, only the central peak values given by that reference are used in the SED. The beam sizes at the available frequencies are 6×5.4 arcsec^2 at 20 cm, 3.4×3.1 arcsec^2 at 13 cm, 1.4×1.3 arcsec^2 at 6 cm and 0.9×0.8 arcsec^2 at 3 cm.

Mid-IR nuclear fluxes are taken from VLT/VISIR diffraction-limited images at 11.9 and 18.7 μm (Reunanen et al. 2009). Further mid-IR data are taken from VLTI/MIDI interferometry spectra covering the 8–13 μm range (Tristram et al. 2007). Two sets of MIDI data are included in the SED: the correlated fluxes, which correspond to an unresolved source detected with a visibility of 10 per cent, and the total fluxes that are measured within the MIDI

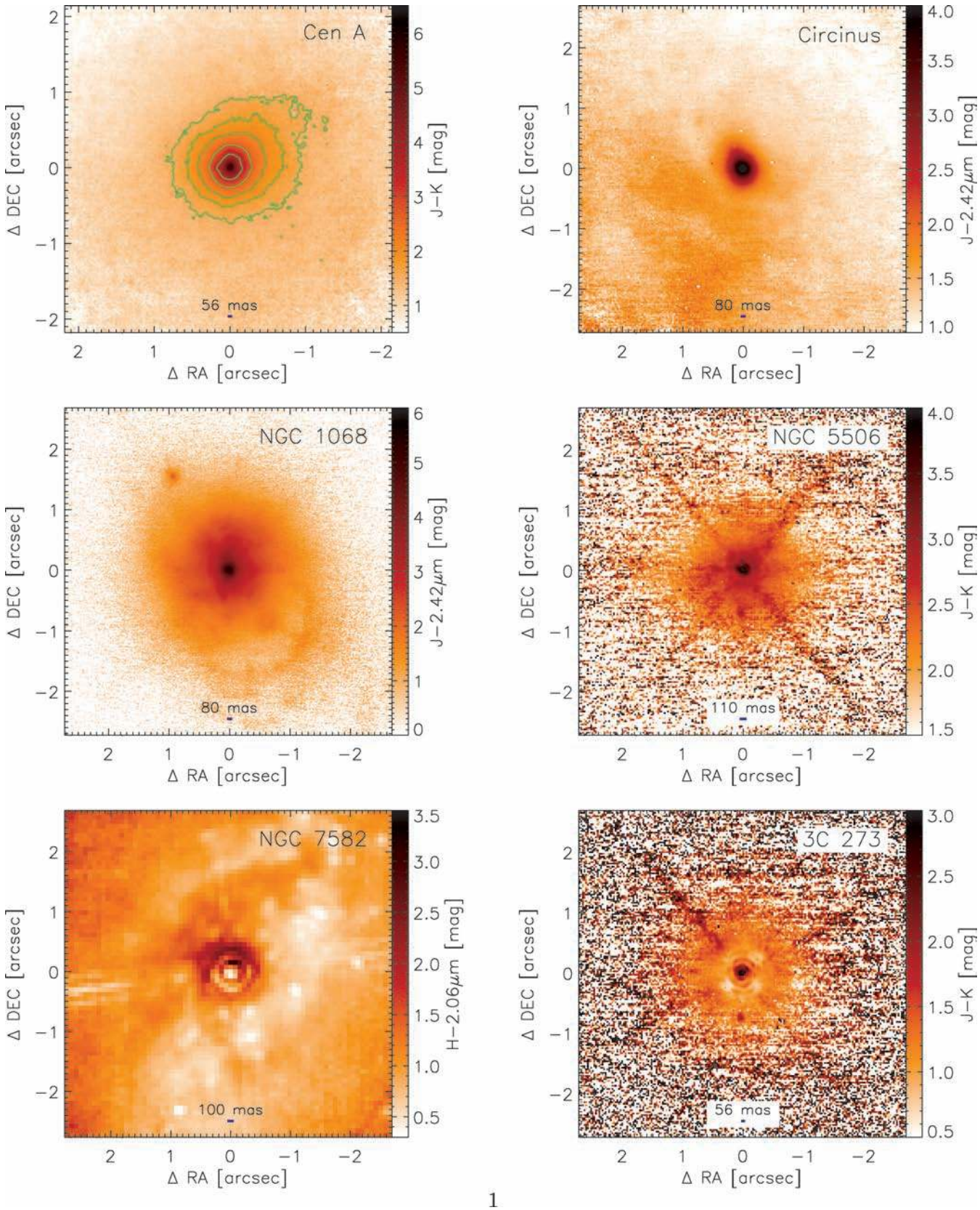

Figure 2. Near-IR colour maps of the galaxies in this study. Most are $J - K$ or J – narrow-band K maps when available. Only the very central 2–3 arcsec radius FoV is shown. The small bar at the bottom of each panel indicates the spatial resolution of the maps and in turn the upper limit size to the AGN core in the K band. Contours are over-plotted on some galaxies to help visualize the colour map structure.

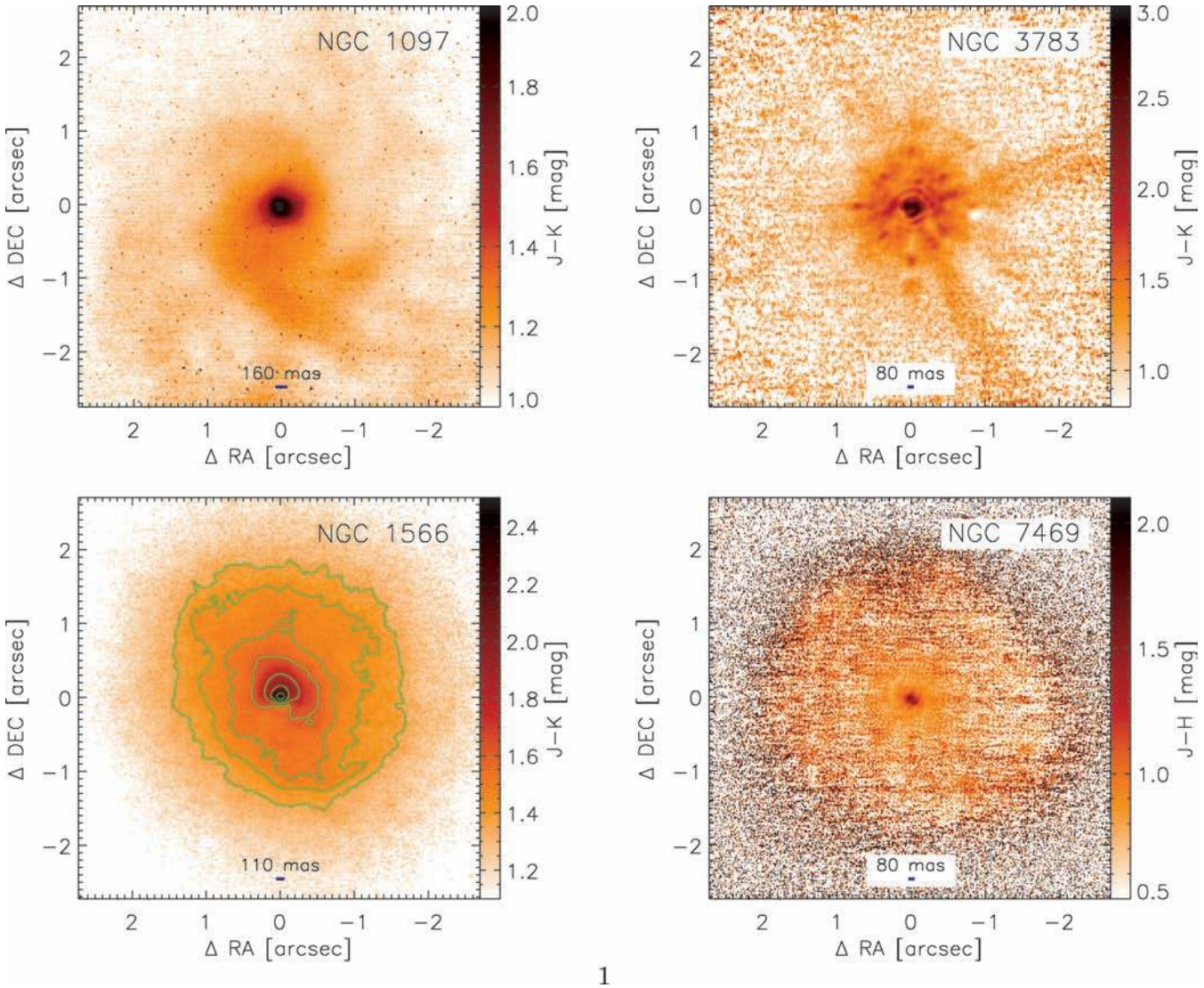

Figure 2 – *continued*

0.52×0.62 arcsec^2 slit. In the latter case, only fluxes at 8 and 9.6 μm are included. For sake of simplicity, flux measurements at the longer MIDI wavelengths are not included as they are in very good agreement with the VISIR flux at 11.9 μm within 5 per cent. Near-IR nuclear fluxes, in the 1–5 μm range, are taken from VLT/NACO adaptive optics images by Prieto et al. (2004). Shortwards of 1 μm, Circinus's nucleus is undetected; an upper limit at 1 μm derived from the NACO *J*-band image is included in the SED.

At the high energies, the SED includes the *ROSAT* 1 keV flux after correction for the hydrogen column density, derived by Contini,

Table 11. Galaxies observed with adaptive optics in the near-IR with VLT/NACO.

Name	Filters (observing date)	Reference
Cen A	*J*, *H*, *NB*-2.02 μm, *L* (2003 March–May), *K* (2004 March)	Haering-Neumayer et al. (2006)
Circinus	*J*, *K*, *NB*-2.42 μm, *L*, *M* (2003 March–May)	Prieto et al. (2004)
NGC 1068	*K*, *M* (2002 November–December), *J*, *H* (2004 January) *J*, *NB*-2.42 μm (2005 January)	Hoenig et al. (2008)
NGC 7582	2.06 μm (2005 May–June), *L*, *NB*-4.05 μm (2005 December)	Fernandez-Ontiveros et al. (in preparation)
NGC 5506	*J*, *K*, *L*, *M* (2003 June)	This work
NGC 1097	*J*, *H*, *K* (2002 August), *L* (2005 January)	Prieto et al. (2005)
NGC 1566	*K*, *L* (2005 January), *J* (2005 November)	This work
NGC 3783	*J*, *K*, *L* (2005 January)	This work
NGC 7469	*J*, *H*, *K* (2002 November), *L*, *NB*-4.05 μm (2005 December)	This work
3C 273	*J*, *K*, *L*, *M* (2003 May)	This work

Note. Galaxies sorted by distance.

Table 12. Extinction towards the nucleus: comparative.

Name	A_V $J-K$	A_V 9.6 μm	A_V N_H
Type 2			
Cen A	5	14	62
Circinus	6	21	Compton-thick
NGC 1068	10–12	7–30	Compton-thick
NGC 7582	9	20	>70
NGC 5506	5	15	17
LINER			
NGC 1097	1	–	–
Type 1			
NGC 1566	7	–	–
NGC 3783	≤0.5	–	–
NGC 7469	–	–	–
3C 273	–	–	–

Note. A_V derived from $J-K$ maps: nuclear extinction relative to that in the galaxy within the central kpc region (see text); A_V from the optical depth at the silicate 9.6 μm feature is derived from MIDI spectra in Cen A (Meisenheimer et al. 2007), Circinus (Tristram et al. 2007) and NGC 1068 (Raban et al. 2009) and from TIMMI2 spectra in NGC 5506 and NGC 7582 (Siebenmorgen et al. 2004). In NGC 3783, no silicate feature in the interferometric MIDI spectrum is apparent (Beckert et al. 2008). No report on the silicate optical depth was found for the remaining sources. The standard dust-to-gas ratio is applied to infer the extinction from the X-ray N_H. For those with no entry, the Galaxy N_H is assumed in their X-ray fit. References to N_H are given in the caption to Table 13.

Prieto & Viegas (1998), and *INTEGRAL* fluxes at different energy bands in the 2–100 keV range (Beckmann et al. 2006).

For comparative purposes, the SED includes large aperture data in the mid-to-far-IR region selected from *IRAS* (Moshir et al. 1990).

There are no reports on significant variability in Circinus at near-IR wavelengths. In comparing the data analysed in this work, we find that the 12 μm nuclear flux measured in 2002 by Siebenmorgen et al. (2004) and that of VLT/ VISIR collected 4 yr apart differ by less than 5 per cent. At the high energies, in the 20–40 keV range, Soldi et al. (2005) report a 10 per cent maximum variability in a time interval of 2 d.

An estimate of the extinction towards the nucleus is derived from the VLT/NACO $J-2.42$ μm colour map (Fig. 2). In the surroundings of the nucleus, $J-2.42\,\mu m > 2.2$ is found. The colours become progressively bluer with increasing distance and in relatively clean patches in the central 150 pc radius the average value is $J-2.42\,\mu m \sim 1$. The comparison of the colours yields a relative extinction of $A_V \sim 6$ mag, assuming a foreground dust screen. Because of the finest scales, a few parsecs, at which Circinus's nucleus is studied, Prieto et al. (2004) further considered a simple configuration of the dust being mixed with the stars, in which case an extinction of $A_V \sim 21$ mag is found. This value is more in line with the range of extinctions derived from the optical depth of the 9.6 μm silicate feature measured in the VLTI/MIDI-correlated spectrum, $22 < A_V < 33$ mag (Tristram et al. 2007).

2.3 NGC 1068

NGC 1068, Circinus and Cen A are the brightest Seyfert nuclei in the sample but NGC 1068 is a factor of 4 further away, at a distance of 14.4 Mpc (Bland-Hawthorn et al. 1997). The adopted scale is 1 arcsec ∼ 70 pc.

NGC 1068's radio core – identified with the radio source S1 – is resolved at 5 and 8.4 GHz into an elongated, ∼0.8 pc disc-like structure, oriented perpendicular to the radio jet axis (Gallimore et al. 2004). VLTI/MIDI interferometry in the 8–12 μm range resolves the nucleus into two components: an inner component of about 1 pc size and a cooler, 300 K disc-like component, with a size of 3 × 4 pc^2 (Raban et al. 2009). At 2 μm speckle observations by Weigelt et al. (2004) resolve the central emission into a compact core with a size of 1.3 × 2.8 pc^2, and north-western and south-eastern extensions. Shortwards of 1 μm, and on the basis of the SED discussed below, NGC 1068's nucleus is fully obscured.

The highest spatial resolution SED of NGC 1068's nucleus from radio to optical is presented in Hoenig, Prieto & Beckert (2008). The authors provide a fair account of the continuum spectrum from radio to IR to optical SED, by including in their model the major physical processes that must contribute to the integrated core emission: synchrotron, free–free emission from ionized gas and the dust-torus emission. The SED included here is that presented in Hoenig et al. but further complemented with high-energy data. Furthermore, the IR nuclear photometry is extracted in a different way: the nucleus of NGC 1068 in the mid-to-near-IR presents additional emission structure extending, particularly, north and south of it (Bock et al. 2000; Rouan et al. 2004). To minimize the contamination by this extended emission, the near-IR nuclear fluxes are extracted here within an aperture diameter comparable with the nuclear FWHM measured at the corresponding wavelength.

The SED is shown in Fig. 1 (Table 3). The radio data are taken from VLA observations at 43 GHz with a 50 mas beam (Cotton et al. 2008) and 22 GHz with a 75 mas beam from Gallimore, Baum & O'Dea (1996), VLBA observations at 8.4 and 5 GHz from Gallimore et al. (2004) and VLBA at 1.7 GHz from Roy et al. (1998). 1 and 3 mm core fluxes are taken from Krips et al. (2006), and correspond to beam sizes larger than 1 arcsec; thus, they may include the contribution from the jet. We still include these data in the SED as the jet components have a steep spectrum (Gallimore et al. 2004), and thus their contribution to the core emission is expected to decrease at these frequencies.

In the mid-IR, the nuclear fluxes in the 8–18 μm range are from Subaru (Tomono et al. 2001), complemented with an additional nuclear flux at 25 μm from Keck (Bock et al. 2000). All these measurements are extracted from deconvolved images in aperture diameters of ∼200 mas. Despite the uncertainties intrinsic to the deconvolution process, we note that the fluxes derived by both group of authors at common wavelengths, each using different instrumentation and telescope, differ by <30 per cent. The SED also includes the 8–12 μm VLTI/MIDI-correlated spectrum of the unresolved component sampled at four wavelengths. This correlated spectrum was derived from a 78 m baseline which provides a spatial resolution of about 30 mas (Jaffe et al. 2004). The total flux measured in the MIDI 500 mas slit render fluxes larger by a factor of 2 than those measured by Bock et al. and Tomono et al. in their 200 mas aperture. This difference is due to the inclusion of the light contribution from the nuclear extended emission of NGC 1068, as mentioned above, in the MIDI slit. Thus, the MIDI total fluxes are not included in the SED. Near-IR data, in the 1–5 μm range, are from VLT/NACO adaptive optics images at J, H, K, M bands and the 2.42 μm narrow-band line-free filter. The nucleus is unresolved at the resolutions achieved; the nuclear fluxes were extracted in aperture diameter comparable to the nucleus FWHM: 0.1 arcsec in J, K and 2.42 μm bands, 0.22 arcsec in the H band

and 0.16 arcsec in the *M* band. The inspection of the VLT NACO *J*-band image indicates a relatively faint source at the position of the *K*-band nucleus, and thus we take the extracted *J*-band flux as an upper limit.

In the X-ray, the following measurements are included in the SED: *Chandra* 1 keV flux from Young, Wilson & Shopbell (2001), *European X-ray Observatory Satellite (EXOSAT)* flux in the 2–10 keV range by Turner & Pounds (1989) and *INTEGRAL* data in the 20–40 keV and 40–100 keV bands from Beckmann et al. (2006).

The SED includes large aperture data in the mid-to far-IR from *IRAS* (Sanders et al. 2003) and *ISO* (Stickel et al. 2004) and in the submillimetre from Hildebrand et al. (1977).

Monitoring of the source in the near-IR by Glass (2004) indicates long-term variability, with an increase by a factor of 2 in flux in the period 1970–1995.

Fig. 2 shows the VLT/NACO $J - 2.42\,\mu$m colour map. Contrary to other AGN in the sample, the nuclear region of NGC 1068 presents a lot of emission structure as seen in the colour map. The average colour around the centre is $J - 2.42\,\mu\text{m} \sim 3$, and gets progressively bluer with increasing distance; at ∼150 pc radius, the average colour $J - 2.42\,\mu$m is ∼0.7. Taking this value as intrinsic to the central region of the galaxy, the inferred extinction in the surrounding of the nucleus is $A_V \sim 10$– 12 mag (Table 12). For comparison, the extinction derived from the depth of the silicate feature in the VLTI/MIDI-correlated spectrum is $A_V \sim 7$ mag for the more external, 3×4 pc cooler component, in rather good agreement with the extinction in the nuclear surrounding. Conversely, the extinction derived for the hotter parsec-scale inner component is $A_V \sim 30$ mag (Raban et al. 2009).

2.4 NGC 1097

NGC 1097 is one of the nearest LINER/Seyfert type 1 galaxy in the Southern hemisphere, at a comparable distance as NGC 1068. The adopted scale is 1 arcsec ∼ 70 pc (distance = 14.5 Mpc; Tully 1988). The nucleus is visible at all wavelengths from UV to radio. In the IR, it is unresolved down to the highest resolution achieved in this object with VLT/NACO: FWHM ∼ 0.15 arcsec in the *L* band (<11 pc).

The SED is shown in Fig. 1 (Table 4). At radio waves, the following measurements are included in the SED: subarcsec resolution data from the VLA-A array at 8.4 GHz (Thean et al. 2000) and at 8.4 GHz, the latter with a beam resolution of 0.66×0.25 arcsec^2 (Orienti & Prieto 2009); VLAB array data at 1.4 GHz with a beam resolution of 2.5×1.5 arcsec^2 (Hummel, van der Hulst & Keel 1987) and VLA-B array archived data at 15 GHz re-analysed in Orienti & Prieto (2009) and for which a final beam resolution of 1.15×0.45 arcsec^2 is obtained. Despite the relatively larger beam of the VLA-B array data, we believe the associated nuclear fluxes to be fully compatible with those derived with the finer scale VLA-A array data. This is based on the analysis of equivalent VLA-A and VLA-B array data at 8.4 GHz which yielded the same nuclear fluxes, indicating that the nucleus is unresolved.

The mid-IR is covered with diffraction-limited resolution data from the VLT/VISIR images at 11.88 and 18.72 μm (Reunanen et al. 2009). The near-IR, 1–4 μm, is covered with VLT/NACO adaptive optics images at *J*, *H*, *K* and *L* bands, which have spatial resolutions FWHM ≤ 0.2 arcsec (Prieto et al. 2004, and this work).

Optical and UV data were extracted from archival *HST*/WFPC2 F220W and F555W images and *HST*/Advanced Camera for Survey (ACS) F814W image. Further UV data available from *International Ultraviolet Explorer* (*IUE*) and *Galaxy Evolution Explorer* (*GALEX*) were not considered as their spatial resolution beams; 20 and 6 arcsec FWHM, respectively, include emission from the prominent NGC 1097's star-forming ring located at 5 arcsec radius from the centre.

In the X-rays, the absorption-corrected fluxes derived by Terashima et al. (2002) in the *Advanced Satellite for Cosmology and Astrophysics (ASCA)* 0.1–4 keV and 2–10 keV windows are used. Further observations at higher energies were not found in the literature.

For comparison purposes, the SED includes large aperture data, for the mid-IR to the millimetric wavelengths, from *IRAS*, *Spitzer* and SCUBA, all taken from Dale et al. (2007).

NGC 1097 has shown variability in the optical, exhibiting broad emission lines. To our knowledge, there is no report on variability at any other spectral range.

Using the VLT/NACO colour maps $J - H$ and $H - K$, Prieto, Maciejewski & Reunanen (2005) estimate a moderate extinction of $A_V \sim 1$ mag towards the centre. To estimate this extinction, the colours in the surrounding of the nucleus were compared with those at further locations, inside the circumnuclear star-forming ring and not contaminated by the nuclear dust filaments. These filaments are readily seen in the NACO $J - K$ colour map shown in Fig. 2.

2.5 NGC 5506

This is a Seyfert type 1.9 nucleus in an edge-on disc galaxy and largely covered by dust lanes. As is found in our VLT/NACO adaptive optics images, the nucleus dominates the galaxy light at IR wavelengths from 1 μm onwards, but there is no equivalent counterpart in *HST* optical images (Malkan, Gorjiam & Tam 1998). In the 1–20 μm range, the nucleus is unresolved down to the best spatial resolution achieved with the NACO observations, that is the *K* band which sets an upper limit for the size of the source of FWHM ∼ 0.10 arcsec (<13 pc). The adopted scale is 1 arcsec ∼ 126 pc [redshift taken from the NASA/IPAC Extragalactic Database (NED)].

The SED is shown in Fig. 1 (Table 5). VLBA maps show the nuclear region resolved in three blobs. In the SED, the emission from the brightest and smallest of the three blobs, also with the flattest spectral index ($\alpha = +0.06$), called the BO component in Middelberg et al. (2004), is taken into account. Reported peak values from VLBA and VLBI at 8.3, 5 and 1.7 GHz, with some of them taken at multiple epochs, are all included in the SED. In addition, Parkes Tidbinbilla Interferometer (PTI) data at 2.3 GHz from Sadler et al. (1995) from a 0.1 arcsec beam is also included.

In the mid-IR, the extracted nuclear fluxes from VLT/VISIR diffraction-limited data at 11.8 and 18.7 μm from Reunanen et al. (2009) are included. Additional fluxes at 6 and 9.6 μm were directly measured on the 6–13 μm spectrum published in Siebenmorgen et al. (2004, their fig. 15), which combines ESO/TIMMI2 and ISO Imaging Photopolarimeter (ISOPHOT) data. Although the ESO/ TIMMI2 data correspond to a 1.2 arcsec slit-width, it perfectly joins the large aperture ISOPHOT spectrum; thus, the measured fluxes should be rather representative of the pure nuclear emission. The near-IR 1–4 μm data are extracted from the VLT/NACO adaptive optics images. As the images are dominated by the central source with bare detection of the host galaxy, the nuclear fluxes were integrated within aperture sizes of 0.5 arcsec in diameter.

Below 1 μm, the nucleus is undetected; an upper limit in the *R* band derived from *HST*/WFPC2 archive images is set as a reference in the SED. In the X-rays, *INTEGRAL* fluxes in the 2–100 keV range

from Beckmann et al. (2006) are included. The soft X-rays, 0.2–4 keV, are covered with *Einstein* data (Fabbiano, Kim & Trinchieri 1992).

For comparison purposes, large aperture data from the mid-to far-IR, collected with *IRAS* (Sanders et al. 2003), are included in the SED.

There is no apparent nuclear variability in the IR over a time-scale of years. This follows from the existing agreement between ISOPHOT, *IRAS*, ground-based spectra taken in 2002 (Siebenmorgen et al. 2004) and VLT/VISIR data taken in 2006; all these data having very different spatial resolutions. The nucleus is however highly variable in the X-rays by factors of ~ 2 in scales of a few minutes (Dewangan & Griffiths 2005).

Fig. 2 shows a VLT/NACO $J - K$ colour image of the central 2.5 kpc region. The nucleus and diffraction rings are readily seen; these are further surrounded by a diffuse halo sharply declining in intensity. Taken as a reference $J - K \lesssim 1.8$ as the average colour in the outermost regions in this halo, $\sim$150 pc radius, and $J - K \sim 2.8$ as that in the surrounding of the nucleus, the comparison of both yields a relative extinction towards the centre of $A_V \geq 5$ mag. Due to the faintness of the galaxy, the true extinction around the nucleus might be much higher than that. Most probably, the colour of the halo is largely affected by the nucleus point spread function (PSF) wings. For comparison, the extinction derived from the depth of the silicate feature at 9.6 μm in Siebenmorgen et al.'s 1.2 arcsec slit-width spectrum is $A_V \sim 15$ mag (Table 12).

2.6 NGC 7582

This is a Seyfert type 2 nucleus surrounded by a ring of star-forming regions. The east side of the galaxy is largely obscured by dust lanes. These fully obscure the nucleus and many of the star-forming regions at optical wavelengths. Most of them and a very prominent nucleus are revealed in seeing-limited VLT/Infrared Spectrometer and Array Camera near-IR images (Prieto, Reunanen & Kotilainen 2002). The spatial resolution achieved in the current adaptive optics images allows for very accurate astrometry on the position of the nucleus, by taking as a reference the star-forming regions identified in both the IR and *HST* optical images. In this way, a weak optical counterpart source at the IR nucleus location is found, along with a rich network of new star-forming regions, some as close as 0.5 arcsec (50 pc) to the centre and the farthest being seen up to about a radius of 320 pc. The ages and masses of these regions are analysed in Fernandez-Ontiveros et al. (in preparation). The nucleus is unresolved down to the best resolution achieved in these observations, which yield an FWHM ~ 0.1 arcsec ($<$11 pc) at 2 μm. The adopted scale is 1 arcsec $\sim$ 105 pc (taking the redshift from the NED).

The SED is shown in Fig. 1 (Table 6). The published radio maps at 8.4 and 5 GHz obtained with the VLA-A array show a diffuse nuclear region (e.g. Thean et al. 2000). In an attempt to improve the spatial resolution, an unpublished set of VLA-A array data at those frequencies was retrieved from the VLA archive and analysed by filtering out the antennas that provide the lowest resolution. In this way, a nuclear point-like source and some of the surrounding star-forming knots could be disentangled from the diffuse background emission. The final beam resolution corresponds to FWHM $= 0.65 \times 0.15$ arcsec^2 at 8.4 GHz and 0.96×0.24 arcsec^2 at 5 GHz (Orienti & Prieto 2009). The radio data used in the SED correspond to the nuclear fluxes extracted from these new radio maps. There is no further high-resolution radio data available for this galaxy.

Mid-IR nuclear fluxes are taken from the analysis done on diffraction-limited VLT/VISIR images at 11.9 and 18.7 μm by Reunanen et al. (2009). Additional measurements in the 8–12 μm range are extracted from an ESO/TIMMI2 nuclear spectrum taken with a 1.2 arcsec slit-width (Siebenmorgen et al. 2004). Although within this slit-width the contribution from the nearest circumnuclear star-forming regions is certainly included, the derived fluxes follow the trend defined by the higher spatial resolution VISIR and NACO data, which indicates the relevance of the AGN light within at least 50 pc radius (0.6 arcsec) from the centre. In the near-IR, 1–4 μm, the nuclear fluxes are extracted from an *HST*/Near-Infrared Camera and Multi-Object Spectrometer (NICMOS) H-band image and the VLT/NACO narrow-band images at 2.06 μm and 4.05 μm, and an L-band image, using aperture diameters of 0.3 arcsec. This aperture is about twice the average FWHM resolution obtained in the NACO images. In the optical, NGC 7582's nucleus becomes very absorbed. We find a weak optical counterpart to the K-band nucleus in the *HST*/ WFPC2 F606W image (Malkan et al. 1998). The estimated flux was derived by integrating the emission in an aperture size of 0.3 arcsec in diameter centred at the location of the IR nucleus.

A bright nuclear source becomes visible again at the higher energies. The nuclear fluxes included in the SED are extracted from *SAX* data in the 10–100 keV band (Turner et al. 2000) and *XMM* data in the 2–12 keV band (Dewangan & Griffiths 2005). In the latter case, the reported absorption-corrected flux is used. An additional soft X-ray flux is extracted from the *ASCA* 0.25–2 keV band-integrated flux, not corrected by absorption, reported by Cardamone, Moran & Kay (2007).

For comparison purposes, large aperture data in the mid-to far-IR from *IRAS* (Sanders et al. 2003) are also included.

NGC 7582's nucleus has shown variability in the optical, exhibiting broad emission lines. It is also variable in the X-rays by factors of 2 in intensity on scales of months to years (Turner et al. 2000). There is no reported variability in the IR. On the basis of the mid-IR data used in this work, the inferred nuclear fluxes from TIMMI2 and VISIR observations collected in 4 yr are in excellent agreement.

An $H - 2.06$ μm colour map is shown in Fig. 2. This is constructed from *HST*/NICMOS H-band and VLT/NACO narrow-band images at 2.06 μm. The central kpc region shown in the map reveals multiple star-forming knots interlaced with dust. The average colour within a radius of 180 pc from the centre and outside the star-forming knots is $H - 2.6$ μm ~ 1.6. Further out, beyond 400 pc radius and avoiding the dust filaments, the average colour is $H - 2.02$ μm ~ 0.9. The relative extinction towards the centre is estimated to be $A_V \sim 9$ mag (Table 12). The depth of the silicate feature at 9.6 μm points to larger values: $A_V \sim 20$ mag (Siebenmorgen et al. 2004).

2.7 NGC 1566

NGC 1566 is a Seyfert type 1 nucleus at a distance of 20 Mpc (Sandage & Bedke 1994). Accordingly, the adopted scale is 1 arcsec $\sim$ 96 pc. The *HST*/ WFPC2 images (e.g. Malkan et al. 1998) show dust lanes circumscribing the nuclear region. Some of them can be followed up to the centre, where they seem to bend and spiral about. The near-IR VLT/NACO diffraction-limited images reveal a smooth galaxy bulge, but some of the innermost dust lanes still leave their mark even at 2 μm. At both near- and mid-IR wavelengths, the nucleus is unresolved down to the best resolution achieved, FWHM < 0.12 arcsec in the K band (11 pc).

The SED is shown in Fig. 1 (Table 7). The HSR radio data are taken form ATCA observations at 8.4 GHz with a beam resolution FWHM = 1.29×0.75 arcsec^2 (Morganti et al. 1999) and from PTI at 2.3 and 1.7 GHz with a beam resolution FWHM < 0.1 arcsec (Sadler et al. 1995). In the mid-IR, the nuclear fluxes are extracted from VLT/VISIR diffraction-limited images at 11.9 and 18.7 μm (Reunanen et al. 2009). In the near-IR, these are extracted from VLT/ NACO adaptive optics images in J , K and L bands, within an aperture diameter of 0.4 arcsec. UV fluxes, in the 1200–2100 Å range, were directly measured on the recalibrated pre-Corrective Optics Space Telescope Axial Replacement *HST*/Faint Object Spectrograph (FOS) nuclear spectra published by Evans & Koratkar (2004). These fluxes were measured on the best possible line-free spectral windows. FOS spectra were collected with the circular 0.26 arcsec aperture diameter. Optical nuclear fluxes were extracted from *HST*/WFPC2 images with filters F160BW, F336W, F547M, F555W and F814W. The X-ray data are from *BeppoSAX* in the 20–100 keV range (Landi, Malizia & Bassani 2005) and from *Einstein* in the 0.2–4 keV range (Fabbiano et al. 1992). In the latter case, an average of the two reported measurements is used. Large aperture data in the mid- and far-IR are from *IRAS* (Sanders et al. 2003) and the flux at 160 μm is from *Spitzer* (Dale et al. 2007).

This nucleus may be variable by about 70 per cent in the X-rays (see Landi et al. 2005) but seems quieter in the optical and the near-IR. Variability by a factor of at most 1.3 over a 3 yr monitoring period is reported in the near-IR, with the optical following a similar pattern (Glass 2004).

A VLT/NACO $J - K$ colour map is presented in Fig. 2. On the basis of this map, the average colour in the surrounding of the nucleus is $J - K \sim 1.5$, the colours get bluer with increasing distance and at about 300 pc radius, the average colour in regions outside the dust filaments is $J - K \sim 0.3$. The comparison of both implies an extinction towards the nucleus of $A_V \sim 7$ mag (Table 12).

2.8 NGC 3783

NGC 3783 is a Seyfert type 1 nucleus in an SBa galaxy. The adopted scale is 1 arcsec $\sim$ 196 pc (redshift taken from the NED). The optical *HST* ACS images show a prominent nucleus surrounded by fingers of dust (also seen in the *HST*/WFPC2 F606W image by Malkan et al. 1998), a bulge and a star-forming ring at about 2.5 kpc radius from the centre. In the near-IR VLT /NACO images, the emission is dominated by an equally prominent nucleus within a smooth and symmetric bulge; the star-forming ring just gets outside the field of view (FoV) of these images. An upper limit to the size of the nuclear region is FWHM < 0.08 arcsec (16 pc) at 2 μm. New results with VLTI/MIDI interferometry are consistent with a resolved central structure with size of $\sim$3.5 pc at 10 μm (Krishimoto et al. 2009).

The SED is shown in Fig. 1 (Table 8). It includes VLA data at 8.4 GHz (FWHM ≤ 0.25 arcsec; Schmitt et al. 2001), at 4.8 GHz (FWHM ~ 0.4 arcsec; Ulvestad & Wilson 1984) and at 1.4 GHz (FWHM $\sim$1 arcsec^2; Unger et al. 1987). VLT/VISIR diffraction-limited data at 11.9 and 18.7 μm from Reunanen et al. (2009) cover the mid-IR range. In the near-IR, 1–4 μm, the nuclear fluxes are extracted from our VLT/NACO adaptive optics images in the J, K and L bands using apertures of $\sim$0.4 arcsec diameter. In the optical, nuclear-aperture photometry was extracted from archived *HST* ACS images taken with filters F547M and F550M and the WFPC2 image with filter F814W. The UV range is covered with archival *HST*/Space Telescope Imaging Spectrograph (STIS) spectra in the 1100–3200 Å region. Continuum fluxes were measured on best possible line-free regions. As NGC 3783's nucleus is very strong, we decided in this case to supplement the SED with additional UV measurements from larger aperture data, specifically from the *Far Ultraviolet Spectroscopic Explorer* (*FUSE*) spectrum published in Gabel et al. (2003) – we measured a data point at $\sim$1040 Å on their estimated continuum flux level in their fig. 1 – in a U-band measurement in a 9.6 arcsec aperture from the Las Campanas 0.6 m telescope reported in McAlary et al. (1983).

In the high-energy range, nuclear fluxes at specific energies were extracted from observations with OSSE in the 50–150 keV range (Zdziarski, Poutanen & Johnson 2000), *INTEGRAL* in the 17–60 keV range (Sazonov et al. 2007), *XMM* in the 2–10 keV range – where the reported flux from the averaged spectrum of several observations in Yaqoob et al. (2005) was used – and *Einstein* in the 0.2–4 keV range (Fabbiano et al. 1992).

Large aperture data in the mid-to-far IR are from *IRAS* (Moshir et al. 1990).

NGC 3783 is known to be variable in the optical and the near-IR by factors of up to 2.5 in intensity on the scale of months (Glass 2004) and on scales of minutes by a factor of 1.5 in the X-rays (Netzer et al. 2003).

A VLT/NACO $J - K$ colour map of the central 1.5 kpc region is shown in Fig. 2. The nucleus is the most prominent feature; this appears surrounded by diffraction rings and atmospheric speckles. The colour distribution is rather flat across the galaxy: $J - K \sim < 1$. The inferred extinction towards the nucleus is moderate: $A_V <$ 0.5 mag. In the VLTI/MIDI interferometric spectrum, the silicate feature at 9.6 μm is absent (Beckert et al. 2008), which is consistent with the derived low extinction.

2.9 NGC 7469

This type 1 nucleus is the most distant source in the sample, 20 times farther than Cen A. The adopted scale is 1 arcsec $\sim$ 330 pc (from the redshift taken from the NED). The nucleus is surrounded by a star-forming ring that extends from 150 to about 500 pc radius (as seen in the *HST*/ACS UV image in Munoz-Marin et al. 2007). The nucleus is unresolved at near-IR wavelengths down to best resolution achieved with VLT/NACO adaptive optic images. This was in the H band, from which an upper limit to the nucleus size FWHM < 0.08 arcsec (26 pc) is derived.

The SED for this source is shown in Fig. 1 (Table 9). This nucleus is known to have undergone a high state level in the optical–UV in the period 1996–2000, followed by a slower return to a low state level reaching a minimum at 2004. Changes in the continuum intensity up to a factor of 4 were measured (Scott et al. 2005). The nucleus is also variable in the X-rays by a factor of 2.5 (Shinozaki et al. 2006). On the other hand, monitoring of the source with *IRAS*-pointed observations in 1983 in a time period of 22 d indicates a stable source at the 5 per cent level (Edelson & Malkan 1987). Accordingly, special attention was paid in selecting the most contemporaneous possible data, with most of them being taken from 2000 onwards. Thus, the SED is based on the following data sources.

The radio regime is covered with PTI data at 1.7 and 2.3 GHz, with a beam size of $\sim$0.1 arcsec (Sadler et al. 1995); Multi-Element Radio-Linked Interferometer Network (MERLIN) data at 5 GHz, with a beam size of $<$0.05 arcsec (Alberdi et al. 2007); and VLA-archived data at 8.4 and 14 GHz, re-analysed in Orienti & Prieto (2009) and for which resolution beams of $<$0.3 arcsec and $<$0.14 arcsec are, respectively, obtained.

In the IR, nuclear fluxes were extracted from VLT/VISIR diffraction-limited images at 11.9 and 18.7 μm collected in 2006 (Reunanen et al. 2009), VLT/ NACO adaptive optics images in J,

H, *K* and *L* bands and the narrow-band continuum filter at 4.05 μm, all collected from 2002 onwards (Table 11), and the *HST*/NICMOS narrow-band continuum image at 1.87 μm, collected in 2007.

In the optical and UV, the nuclear fluxes were extracted from the *HST*/ACS F330W (collected in 2002), F550M and F814W (both in 2006), and WFPC2 F218W (1999) and F547M (2000) images. The aperture size used in all cases, VLT-IR and *HST*–optical–UV, was 0.6 arcsec in diameter. This selection was a compromise between getting most of the light in the nuclear PSF wing and avoiding the star-forming ring.

In the X-rays, nuclear fluxes at specific energies were extracted from observations with *INTEGRAL* in the 17–60 keV band (Sazonov et al. 2007), *XMM* in the 2–10 keV band (Shinozaki et al. 2006) and *ROSAT* in the 0.1–2.4 keV band (Perez-Olea & Colina 1996). In the cases of *XMM* and *ROSAT*, the fluxes included in the SED were derived from the luminosities provided by the authors, and we thus assume that they are intrinsic to the source, although this is not explicitly mentioned to be the case. The *ROSAT* flux is nevertheless not genuine from the nucleus as it includes the contribution of the complete star-forming ring.

The SED is complemented with large aperture data in the IR, taken from *IRAS* (Sanders et al. 2003) and *Spitzer* (Weedman et al. 2005), and millimetre from SCUBA (Dunne et al. 2000) and the Caltech Submillimeter Observatory (Yang & Phillips 2007).

A VLT/NACO $J - H$ colour map of the central 4 kpc region is shown in Fig. 2. This was selected instead of the usual $J - K$ because of the better spatial resolution reached in the *H* band. The map shows the nucleus and a ring of diffuse emission which just encloses the star-forming regions, with a radius of 500 pc. Further out from the ring, the signal in the individual near-IR images drops dramatically and a reliable estimate of the intrinsic galaxy colours is not possible. Thus, an estimate of the relative extinction around the nucleus is not provided in this case. As in NGC 3783, the available VLTI /MIDI interferometric spectra do not show evidence for a silicate feature.

3 COMPARING WITH A QUASAR: THE SED OF 3C 273

3C 273 is one of the most luminous quasars in the sky reaching a luminosity of several 10^{46} erg s^{-1} at almost any energy band. In gamma rays, its luminosity reaches 10^{47} erg s^{-1}, which is suspected to be due to strong beaming at these energies.

3C 273 is a radio-loud source while all the other AGN discussed in this work are radio quiet, with the possible exception of Cen A. It is also the most distant object in the sample: the adopted scale is 1 arcsec $\sim$ 3.2 kpc (redshift taken from the NED). The high power of 3C 273 makes its SED insensitive to the spatial resolution data used at almost any band, except in the low frequency regime where some of the jet components are somewhat comparable to the core strength. This along with its excellent wavelength coverage leads us to use this SED as a reference for a no-obscured AGN. 3C 273 is variable mainly at high energies by factors of 3–4. But from optical to radio, the reported variability is 20–40 per cent (Lichti et al. 1995; Turler et al. 1999), which might affect the SED in detail but has minimal impact on the overall shape.

The SED of 3C 273 is shown in Fig. 1 (Table 10). The data from 1 μm up to the gamma rays are from Turler et al. (1999). These data are indeed an average of multiple observations at distinct epochs. Further in wavelength, the following set of data is used: for consistency with the rest of the work presented here, the data beyond 1 μm up to 5 μm are taken from our VLT/NACO adaptive optics images (collected in 2003 May); the difference with the larger aperture data used in Turler et al. is less than 10 per cent. The 6–200 μm range is covered with *ISO* (collected in 1996; Haas et al. 2003). In the millimetre and radio waves, we used higher resolution data than those in Turler et al. to better isolate the core from the jet components. These are VLBI observations at 3 mm from Lonsdale, Doelman & Phillips (1998) and 147, 86, 15 and 5 GHz from Greve et al. (2002), Lobanov et al. (2000), Kellerman et al. (1998) and Shen et al. (1998), respectively. Additional VLBA measurements at 42 and 22 GHz – peak values – are taken from Marscher et al. (2002).

A VLT/NACO $J - K$ colour map is shown in Fig. 2. This shows the central point-like source and various diffraction rings.

The SED of 3C 273 differs from all those shown in this work mainly in the radio domain, presenting a flatter spectrum as expected from a radio-loud source. In the optical to UV, the difference is also important with type 2 nuclei because of the dust absorption in the latter but less so with type 1s. For comparative purposes, an artificial extinction of $A_V = 15$ mag was applied to the SED of 3C 273 and the result is shown on top of its SED in Fig. 1. With extinction values in this range, which is on average what we measure from the near-IR colour maps in the galaxy sample, the UV to optical region in 3C 273 becomes fully absorbed, presenting a closer resemblance to that shown by the Seyfert type 2 nuclei.

The comparison of 3C 273 with the type 1 nuclei is more illustrative. The average of the three genuine type 1 SEDs compiled in this work is shown together with that of 3C 273 in Fig. 3. The SEDs are normalized to the mean value of their respective power distributions; in this way, they appear at comparable scale about the optical region. All the SEDs show in the optical to UV the characteristic blue-bump feature of type 1 sources and the usual inflection point at about 1 μm. However, whereas the blue bump is stronger in 3C 273, indeed the dominant feature in the UV to IR region, it is weaker and softer in energy in the Seyfert type 1's. Conversely, in the IR the type 1 objects show a broad bump feature in the 10–20 μm range whereas 3C 273 shows a flatter distribution over the same spectral region, the general trend being of a shallow decrease in power with decreasing frequency.

A weaker UV bump is an indication of more dust in the line of sight to these type 1 nuclei, but the lack of the IR bump in 3C 273, which is a key diagnostic of the existence of a central obscuring dust structure in any AGN, points to not much dust in this nucleus. This absence may still be due to a strong non-thermal contribution – this is a flat-spectrum radio source – which would smear out any IR bump. However, this will make the dust contribution to the IR even lower. Some hot dust may still exist in 3C 273, as traced by the detection of silicate features in emission at 10 and 20 μm (Hao et al. 2005). Thus, the overall evidence points to a poor dusty environment in this object as compared with those of lower luminosity AGN. There are also first results with VLTI/MIDI and Keck interferometry on 3C 273 which indicate a slightly resolved nuclear structure at 10 and 2 μm, respectively (Tristram et al. 2009; Pott et al., in preparation). However, it is more plausible that this structure is caused by the jet of 3C 273 rather than by dust.

At the high energies, the comparison of the Seyfert's SED shape with that of 3C 273 is limited by the poorer spectral coverage of the former. Still, in the overlapping region, from the soft X-rays till $\sim$200 keV, the SED of all the Seyfert galaxies presents a gentle rise in power with increasing frequency. This trend may point out to the existence of a further emission bump at much higher energies but may escape detection with present facilities. A broad emission

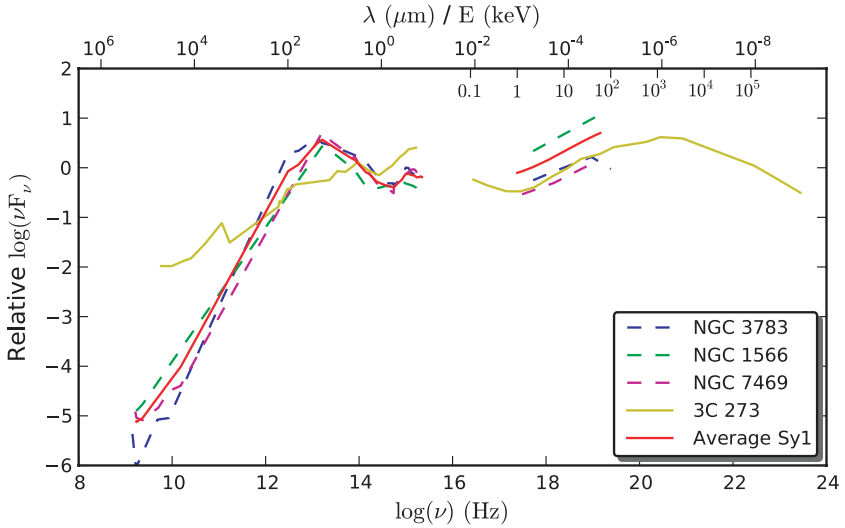

Figure 3. Average SED – in red – of the type 1 nuclei in this work: NGC 1566, NGC 3783 and NGC 7469. 3C 273 – in yellow – is shown for comparison. Prior averaging, each SED was set to its rest-frame system and then normalized to the mean value of its νF_ν distribution. In the X-rays, the average is determined in the energy-window common to the three objects, 1 to ∼60 keV.

bump peaking at the MeV region is detected in both 3C 273 and Cen A with jets detected in the X-rays.

4 RESULTS: THE NEW SED OF NEARBY AGN

4.1 The SED shape

The HSR SEDs (Fig. 1) are all characterized by two main features: an emission bump in the IR and an increasing trend in power at the high energies.

The available HSR data span the UV, optical and IR up to about 20 μm. Shortwards of ∼1 μm, all the type 2 nuclei are undetected or barely detected (e.g NGC 7582). Longwards of 20 μm, there is a wide data gap up to the radio frequencies due to the lack of data of comparable spatial resolution. Subject to these limitations, all type 2 nuclei are characterized by a sharp decay in power from 2 μm onwards to the optical wavelengths. Conversely, type 1 objects also present a decay shortwards of 2 μm but this recovers at about 1 μm to give rise to the characteristic blue-bump feature seen in quasars and type 1 sources in general (e.g. Elvis et al. 1994). The inflection point at about 1 μm is also a well-known feature in AGN, generally ascribed to a signature of dust emission at its limiting sublimation temperature (Sanders et al. 1989). The only LINER in the sample, NGC 1097, appears as an intermediate case between both type 1 and 2: it is detected up to the UV wavelengths but there is no blue bump, its overall SED being more reminiscent of a type 2 nucleus.

Longwards of 2 μm, all the SEDs tend to be flat and there is some hint of a turnover towards lower power at about 20 μm in some objects. The large data gap in the far-IR to the millimetric wavelengths leaves us with the ambiguity on the exact shape of the IR bump and its width. Because of the small physical region sampled in the near- to mid-IR, on the scale of tens of parsec, an important contribution from cold dust at these radii that would produce a secondary IR-millimetre bump is not anticipated. Instead, a smooth decrease in νF_ν towards the radio frequencies is expected. This suggestion follows from the SED turnover beyond 20 μm shown by the objects for which large aperture data in the far-IR or the millimetre wavelengths could be included in their SEDs, namely NGC 3783, NGC 5506 and Cen A.

The complete galaxy sample is detected in the 0.2–100 keV region, with the exception of NGC 1097 for which no reported observations beyond 10 keV were found. All show a general increase in power with frequency. At higher energies, Cen A is the only source detected up to the MeV region. Indeed, among low-power AGN, Cen A is so far the only source detected at gamma rays (Schonfelder et al. 2000). 3C 273 is of course detected at these energies, and both 3C 273 and Cen A exhibit a rather broad bump peaking in the MeV region.

Fig. 4 shows the average of the type 2 SEDs – excluding the case of Cen A because of its non-thermal nature (see Section 6.3) – compared with that of the type 1's (the same average SED shown in Fig. 3). The same procedure to produce the average type 1's is used for type 2's: each type 2 SED is normalized to the mean of its power distribution, the resulting SEDs being then averaged. The resulting average template for each type is plotted one on top of the other in the figure. It can be seen that the most relevant feature in both SED types is the IR bump. This can be reconciled with emission from dust with an equivalent grey-body temperature of ∼300 K in average (Section 4.2). The location and shape of the bump longwards of 2 μm are similar for both types; they are shortwards of this wavelength where the difference arises: type 1s present a shallower 2 μm-to-optical spectrum which is further ensued by the blue-bump emission. This dramatic difference suggests a clearer sight line to hot dust in type 1s but an obscured one in type 2s. This is fully consistent with the torus model: the shallower spectrum reflects the contribution of much hotter dust from the inner region of the torus which we are able to see directly in type 1s; in the type 2s this innermost region is still fully absorbed by enshrouding colder dust.

The second important feature in both SED templates is the high-energy spectrum. Within the common sampled energy band – 0.1 to ∼100 keV – this region appears rather similar in both AGN types, the general trend being that of a gentle increase in power with increasing frequency.

4.2 Core luminosities

Having compiled a more genuine SED for these AGN, a tighter estimate of their true energy output can be derived by integrating

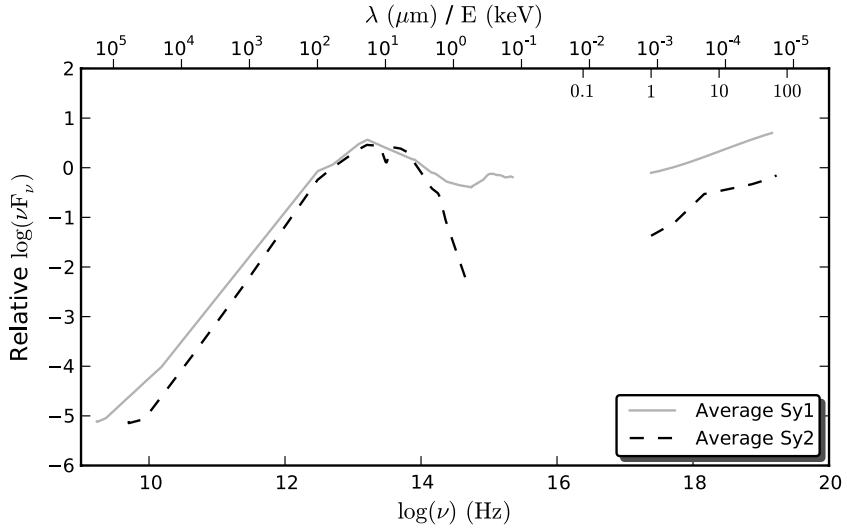

Figure 4. Average SED template of type 1s, in thick line – NGC 3783, NGC 1566 and NGC 7469 – and of type 2s, in dash line – Circinus, NGC 1068, NGC 5506 and NGC 7582. Before averaging, each SED was set to its rest-frame system and then normalized to the mean value of its νF_ν distribution. The average for type 2s in the X-rays is determined in the common energy window of 1–70 keV and that of type 1s in the energy window of 1–60 keV.

the SED. This is done over the two main features in the SED: the IR bump and the high-energy spectrum (Fig. 1). For the type 1 sources, a further integration was done over the blue bump. The estimated energies associated with each of these regions are listed in Table 13. The procedure used is as follows.

The integration over the IR bump extends from the inflection point at about 1 μm in type 1s, from the optical upper limit in type 2s, up to the radio frequencies. Direct numerical integration on the F_ν versus ν plane was done. For those sources whose nuclear flux is independent of the aperture size, namely NGC 5506, NGC 3783 and 3C 273, the integration includes the large aperture IR data as well. For Cen A, the millimetre data were also included. For all other sources, a linear interpolation between 20 μm and the first radio frequency point was applied. Effectively, the proposed integration is equivalent to integrating over the 1–20 μm range only as this region dominates the total energy output by orders of magnitude in all the objects. As a control, a modified blackbody (BB) spectrum, $B_\nu \times \nu^{1.6}$, was fitted to this spectral range. The derived effective temperature converges into the 200–400 K range in most cases, and the inferred IR luminosities are of the same order of magnitude as those derived by the integration procedure over the SED. Focusing on the objects for which their nuclear fluxes are independent of the aperture size – NGC 3783 and NGC 5506 – a further test was done by comparing their integrated luminosity in the 1–20 μm range with that in the 1–100 μm range, the latter including all the available data. The 1–20 μm luminosity is found to be about a factor of 1.5 smaller.

Table 13. Energy budget in nearby AGN. Objects are ordered by increasing IR core luminosity.

Name AGN type	$\mathrm{FWHM_{nucleus}}$ in pc at 2 μm	$L_{\mathrm{IR-HSR}}$ (erg s^{-1})	$L_{\mathrm{X>20\,keV}}$ (erg s^{-1})	L_{total} (erg s^{-1})	$\frac{L_{\mathrm{opt-UV}}}{L_{\mathrm{IR-HSR}}}$ (per cent)	$\frac{L_{\mathrm{IR-HSR}}}{L_{\mathrm{total}}}$ (per cent)	$\frac{L_{IRAS}}{L_{\mathrm{IR-HSR}}}$	L_{IRAS} (erg s^{-1})
NGC 1097/ LI	<11	3.3×10^{41}	5.2×10^{40}	3.8×10^{41}	–	87	500	1.5×10^{44}
Cen A/T2	<1	1.7×10^{42}	1.1×10^{42}	2.8×10^{42}	–	61	20	3.5×10^{43}
NGC 1566/ T1	<11	1.8×10^{42}	3.7×10^{42}	5.5×10^{42}	14	33	78	1.4×10^{44}
Circinus/T2	∼2	8×10^{42}	4.3×10^{41}	8.4×10^{42}	–	82	7	5.5×10^{43}
NGC 7582/ T2	<11	1.3×10^{43}	4.5×10^{42}	1.8×10^{43}	–	72	25	3.2×10^{44}
NGC 1068/ T2	1.2 × 2.8	8.6×10^{43}	6.5×10^{41}	8.7×10^{43}	–	99	9	7.8×10^{44}
NGC 5506/ T2	<13	1.2×10^{44}	6.6×10^{42}	1.3×10^{44}	–	99	1.1	1.3×10^{44}
NGC 3783/ T1	<16	1.6×10^{44}	2.5×10^{43}	1.8×10^{44}	13	89	0.8	1.3×10^{44}
NGC 7469/ T1	<26	2.2×10^{44}	3×10^{43}	2.5×10^{44}	10	88	7	1.5×10^{45}
3C 273/ T1	<180	2.4×10^{46}	5.7×10^{46}	8×10^{46}	90	30	0.8	1.8×10^{46}

Notes. Column 1: object name and AGN type: type 1, 2 and LINER. Column 2: upper limit to the core size at 2 μm, set by the spatial resolution achieved in the *K* band adaptive optics image. Only in Circinus and NGC 1068, the nucleus is resolved at 2 μm; the quoted sizes are from Prieto et al. (2004) and Weigelt et al. (2004), respectively). Column 3: IR luminosity integrated over the HSR data, from radio to the inflection point in the optical. It includes *IRAS* and/or *ISO* data only in the cases of NGC 3783, NGC 5506 and 3C 273 only (see text for details). Column 4: X-ray luminosity from the highest energy range available in the literature. These are as follows: L(20–100 keV) for Cen A, Circinus, NGC 1068 and NGC 5506 (Beckmann et al. 2006) and for NGC 7582 and NGC 1566 (Landi et al. 2005); L(2–10 keV) for NGC 1097 (Terashima et al. 2002); L(17–60 keV) for NGC 3783 and NGC 7469 (Sazonov et al. 2007); L(20–200 keV) for 3C 273, the average of two measurements at different epochs (Lichti et al. 1995). All the luminosities are normalized to $H_0 = 70\,\mathrm{km\,s^{-1}\,Mpc^{-1}}$ when required or to the adopted distance for the nearest objects, namely Cen A, Circinus, NGC 1068, NGC 1097 and NGC 1566 (see Sections 2.1, 2.2, 2.3, 2.4 and 2.7, respectively). Column 5: total luminosity defined as $L_{\mathrm{IR-HSR}} + L_{\mathrm{X(>20\,keV)}}$. Column 6: optical–UV luminosity – blue bump – relative to $L_{\mathrm{IR-HSR}}$. Column 7: IR fraction of the total luminosity. In Columns 8 and 9, L_{IRAS} is the *IRAS* luminosity following Sanders Mirabel's prescription (1996), and effectively accounts for the 8–1000 μm region.

Thus, the IR luminosity is probably underestimated by at least this factor in all other sources.

At high energies, due to energy-band overlapping between different satellites, a direct integration over the SED was avoided. Instead, we used X-ray luminosities reported in the literature, selecting those derived from the hardest possible energy band, usually in the 20–100 keV range. X-ray luminosities above 20 keV are less subjected to absorption and thus expected to be a fair indication of the nuclear budget (with the possible exception of NGC 1068 due to the large X-ray column density, $N(H) > 10^{25}$ cm^{-2}, inferred in this case; Matt et al. 1997).

For the Seyfert type 1 nuclei, the integration over the blue bump spans the 0.1–1 μm region. The same integration procedures described above were applied to 3C 273 as well.

On the basis of these energy budgets, an estimate of the bolometric luminosity in these AGN is taken as the sum of the IR plus X-ray – above 20 keV – luminosities (Table 13). In doing so, it is implicitly assumed that the IR emission is a genuine measurement of the AGN energy output and accounts for most of the optical to UV to X-ray luminosity generated in the accretion disc.

5 THE EXTINCTION GRADIENT TOWARDS THE CENTRE

Table 12 gives a comparison of nuclear extinction values inferred from different methods. A first-order estimate is derived from the near-IR colour maps presented in this work. With these maps, the colours in the surrounding of the nucleus are compared with those at further galactocentric radii, usually at several hundred parsecs. Colour excesses are found to progressively increase towards the central region, an indication of an increasing dust density towards the nucleus. In some cases however the distribution of colours is rather flat, e.g. in NGC 1097, NGC 3783. These central extinctions, in some cases inferred at distances of 30–50 pc from the centre, are systematically lower, by factors of 2–3, than those inferred from the silicate feature at 9.6 μm (Table 12). Considering the very HSR of some of the silicate feature measurements, the difference is an indication that the distribution of absorbers at the nuclear region is not smooth but has a high peak concentration at the very centre.

A further comparison with the optical extinction inferred from the X-rays column density, assuming the standard Galactic dust-to-gas ratio and extinction curve (Bohlin, Savage & Drake 1978), is also given in Table 12. It is known that the extinctions derived in this way are always very large. For the objects in this work, they are several factors, or even orders of magnitude in the Compton-thick cases, higher than those inferred from the silicate feature. Only in NGC 5506, the values derived from both methods agree. Such high discrepancies have to be due to the inapplicability of the Galactic dust-to-gas ratio conversion in AGN environments (see Gaskell et al. 2004).

6 DISCUSSION

6.1 The IR SED: large aperture versus high spatial resolution

We have compiled SEDs at subarcsec scales for a sample of nearby well-known AGN. These SEDs reveal major differences in the IR region when compared with those based on IR satellite data. First, the trend defined by the large aperture IR data (crosses in Fig. 1) is different from that defined by the HSR data (filled points in Fig. 1). Secondly, the true AGN fluxes can be up to an order of magnitude lower than those inferred from large aperture data; hence, the bolometric luminosities based on IR satellite data can be overestimated by orders of magnitude.

The number of objects studied at these HSRs is small. They are however among the nearest AGN. Subjected to this limitation, if we take the new SEDs as a reference for the Seyfert class, the above results have two further implications as follows.

(1) The AGN contribution to the mid-to-far-IR emission measured by e.g. *IRAS*, *ISO*, *Spitzer* is minor; the bulk of the emission measured by these satellites comes from the host galaxy. This result fully confirms previous work by Ward et al. (1987), who pointed out the relevance of the host galaxy light in the *IRAS* fluxes even in type 1 AGN. On this basis the common radio – far-IR correlation followed by both AGN and normal star forming galaxies is understandable (Sopp & Alexander 1991; Ray et al. 1998; Polletta et al. 2007). A common trend indicates that the far-IR emission is unrelated to the AGN. The shape of the HSR SEDs of the sample AGN shows that the large aperture mid-IR is also unrelated in most cases.

(2) The selection or discrimination of AGN populations on the basis of mid-to-far-IR colours may not be applicable on a general basis. For example, de Grijp, Lub & Miley's (1987) criteria were based on the *IRAS* density flux ratio at 60 and 25 μm, $f_{60}/f_{25} > 0.2$, to find mostly AGN. Recently, Sanders et al. (2007) proposed the use of the colour of the *Spitzer* 3.6–24 μm spectrum to help in separating type 1 from type 2 AGN. Considering the shape and luminosity of the HSR SEDs, it is somewhat surprising that large aperture mid-to-far-IR colours may keep track of the existence of a central AGN in most galaxies.

However, the above criteria should apply to cases where the AGN dominates the IR galaxy light in a similar way as in quasars. Two of the HSR SEDs studied reflect this situation: NGC 5506, a type 2 nucleus, and NGC 3783, a type 1 nucleus. In both, large aperture data remain representative of the nuclear emission, as is also the case of quasar 3C 273 used here for comparative purposes. The SEDs of these objects show a smooth connection between the large aperture far- to mid-IR data and the HSR mid- to near-IR data (Fig. 1). In NGC 5506, the nucleus's high contrast in the IR is due to the low surface brightness and edge-on morphology of the host galaxy. However, this is not the case for NGC 3783 which resides in a bright face-on spiral. 3C 273 resides in an elliptical galaxy but as an extreme powerful quasar it dominates the light of its host at any wavelength. The relevance of the AGN in these objects is more obvious in the $J - K$ colour maps shown in Fig. 2. These are dominated by the central source, and almost no trace of the host galaxy at further radii from the centre is detected indicating a flat and smooth galaxy light profile. This morphology is rather different from what is seen in the other AGN in the sample whose colour maps highlight the central dust distribution.

NGC 5506 and NGC 3783 happen to be among the most powerful nuclei in the sample, besides 3C 273, with IR luminosities above 10^{44} erg s^{-1}. The nearest in power is NGC 1068 with $L_{\rm IR} \sim 8.6 \times 10^{43}$ erg s^{-1} (Table 13), a mere factor of 2 lower. Thus, there is a tentative indication that AGN luminosities above 10^{44} erg s^{-1} may easily be traceable in the IR regardless of the aperture flux used. One would expect quasars to naturally comply with this criterion, but the generalization is not that obvious. A third AGN in the sample, NGC 7469, has an IR core luminosity of 2×10^{44} erg s^{-1}, but its host galaxy dominates the total IR budget by a factor of 7 (Table 13).

6.2 Total energy budget: IR versus X-ray luminosities

The nuclear luminosities derived in the IR should provide a tighter quantification of the dust-reprocessed optical to UV and X-rays photons produced by the AGN – the accretion luminosity and X-ray corona. On this premise, an estimate of the total energy budget in these objects as the sum of their IR and hard X-ray emissions is evaluated ($L_{\rm IR} + L_{>20\,\rm keV}$ in Table 13). We compute the same number in type 1s as well, on the assumption that the blue-bump emission visible in these objects is accounted for in the IR-reprocessed emission and thus is not summed up to the total budget (following similar reasoning as in e.g Vasudevan & Fabian 2007). We account for the X-ray contribution for energies above 20 keV as photons beyond this energy should provide a genuine representation of the nucleus plus jet emission.

In comparing the IR and X-ray luminosities in Table 13, the IR luminosity is found to dominate the total budget by more than ∼70 per cent in seven out of the 10 cases studied. Indeed, in most of these cases, the X-ray emission is a few per cent of the total. The three exceptions include Cen A, in the borderline with an IR contribution of about 60 per cent of the total, and 3C 273 and NGC 1566, where the IR contribution reduces to less than 30 per cent of the total. Cen A and 3C 273 are the two sources in the sample with a strong jet, also in the X-rays.

As can be explored from Table 13, there is no dependence of the IR to X-ray ratio on the AGN luminosity but the sample is small. This ratio is furthermore vulnerable to variability. As reported for each object in Section 2, variability in the X-rays is common in these objects, by a factor of 2–3 in average – up to a factor of 10 has been seen in Cen A – whereas variability in the IR is at most a factor of 2, so far only known for Cen A, NGC 1068 and NGC 3783. Thus, X-ray variability which is also faster in time-scales can modify the IR to X-ray ratios up and down by the same factors. Still, even if accounting for a positive increase in the X-ray luminosity by these factors, the IR luminosity remains the dominant energy output for most cases.

Focusing on the Seyfert type 1 objects, all characterized by a blue-bump component in the SED, the luminosity associated with the observable part of this region is ∼15 per cent of the IR luminosity, whereas in 3C 273, integrating over the same spectral region, this is 90 per cent (Table 13). A fraction of the blue-bump energy is unobserved as it falls in the extreme UV to soft-X-rays data gap; still, the fact that there is almost a factor of 6 difference in these relative emissions between 3C 273 and the Seyfert type 1 nuclei is an indication that Seyfert AGN are seen through much more dust. This is in line with conclusions reached by Gaskell et al. (2004) who argue on the presence of additional reddening by dust in radio-quiet as compared with radio-loud AGN. If this is the case, the IR bump luminosity may be one of the most tight measurements of the accretion luminosity in Seyfert galaxies.

6.3 Centaurus A: a special case

Among all AGN analysed in this work, Centaurus A's SED singles out as a particular case. The data points from VLBA over the millimetre to the high-resolution IR measurements follow a rather continuous trend. This region can be fitted by a simple synchrotron model with a spectral index, $F_\nu \sim \nu^{-0.3}$, and the gamma-ray emission can still be explained as inverse Compton scattering of the radio synchrotron electrons (Prieto et al. 2007; see also Chiaberge, Capetti & Celotti 2001). Such a flat synchrotron spectrum has been suggested by Beckert & Duschl (1997, and references therein) for low luminosity AGN, such as Cen A nucleus. The HSR IR observations available indicate that most of the emission comes from a very compact source less than 1 pc in diameter (Meisenheimer et al. 2007). This together with the apparent synchrotron nature of its SED points to a rather torus-free nucleus. Cen A is one of the lowest power sources in the sample, with $L(\rm IR) \sim 10^{42}\,\rm erg\,s^{-1}$. On theoretical grounds, it is being argued that AGN of this low power may be unable to support a torus structure and should thus show a bare nucleus at IR wavelengths (e.g. Elitzur & Shlosman 2006; Hoenig & Beckert 2007). In other respects, Cen A's SED is similar to those of type 2 nuclei in this study, in the sense that its optical to UV is totally obscured but this may be caused by the large-scale dust lanes crossing in front of its nucleus. The future availability of millimetre data of HSR will help to confirm the nature of this SED.

7 CONCLUSIONS

Subarcsec resolution data spanning the UV, optical, IR and radio have been used to construct SEDs of the central, several tens of parsec, region of some of the nearest and brightest AGN. Most of these objects are Seyfert galaxies.

These HSR SEDs differ largely from those derived from large aperture data, in particular in the IR: the shape of the SED is different and the true AGN luminosity can get overestimated by orders of magnitude if based on IR satellite data. These differences appear to be critical for AGN luminosities below $10^{44}\,\rm erg\,s^{-1}$ in which case large aperture data sample in full the host galaxy light. Above this limit we find cases among these nearby Seyfert galaxies where the AGN behaves as the most powerful quasars, dominating the host galaxy light regardless of the integration aperture size used.

The HSR SEDs of these nearby AGN are all characterized by two major features in their power distribution: an IR bump with a maximum in the 2–10 μm range and an increasing trend in X-ray power with frequency in the 1 to ∼200 keV region, i.e. up to the hardest energy that was possible to sample. These dominant features are common to Seyfert type 1 and 2 objects alike.

The major difference between type 1 and 2 in these SEDs arises shortwards of 2 μm. Type 2s are characterized by a sharp fall-off shortwards of this wavelength, with no optical counterpart to the IR nucleus being detected beyond 1–0.8 μm. Type 1s also show a drop shortwards of 2 μm but this is more gentle – the spectrum is flatter – and recovers at about 1 μm to give rise to the characteristic blue-bump feature seen in quasars. The flattening of the spectrum shortwards of 2 μm is also an expected feature of type 1 AGN. Interpreting the IR bump as AGN-reprocessed emission by the nuclear dust, in type 1s the hotter dust located nearest to the centre can be directly seen, hence the flattening of their spectrum, whereas in type 2s this hot dust is still fully obscured.

Longwards of 2 μm, all the AGN types show very similar SEDs; the bulk of the IR emission starts from this wavelength onwards and the shape of the IR bump is very similar in all the AGN. This is compatible with an equivalent BB temperature for the bulk of the dust in the 200–400 K range in average. Although the current shape of the IR bump is limited by the availability of high angular resolution data beyond 20 μm for most objects, due to the small region sampled in these SEDs, of just a few parsecs in some galaxies, a major contribution from colder dust that will modify the IR bump is not expected.

It can thus be concluded that at the scales of a few tens of parsec from the central engine, the bulk of the IR emission in either AGN type can be reconciled with pure dust emission. It follows that further contributions from a non-thermal synchrotron

component and/or a thermal free–free emission linked to cooling of ionized gas are insufficient to overcome that of dust at these physical scales. The detailed modelling of NGC 1068's SED – this being one of the most complete we have compiled – in which these three contributions – synchrotron, free–free and dust torus components – are taken into account illustrates that premise, that is, the dominance of dust emission in the IR, even at the parsec-scale resolution achieved for this object in the mid-IR with interferometry (Hoenig et al. 2008). Only the two more extreme objects in this analysis, Cen A, on the low luminosity rank, and 3C 273, on the highest, present an SED that is not dominated by dust but by a synchrotron component. We tend to believe that is due to a much reduced dust content in these nuclei.

Over the nine orders of magnitude in frequency covered by these SEDs, the power stored in the IR bump is by far the most energetic fraction of the total energy budget measured in these objects. Evaluating this total budget as the sum of the IR and hard X-ray – above 20 keV – luminosities, the IR part accounts for more than 70 per cent of the total in seven out of the 10 AGN studied. In the three exceptions, the IR fraction reduces to $\leq$30 per cent of the total in 3C 273 and NGC 1566, and $\leq$ 60 per cent in Cen A. Even if accounting for variability in the X-rays, by a factor 2 to 3 in average, the IR emission remains in all cases dominant over, or as important as in the last three cases, the X-ray emission. If we compare this with the observed blue-bump luminosity in the type 1 nuclei, then this represents less than 15 per cent of the IR emission. Putting all together, the IR bump energy from these HSR SEDs may represent the tightest measurement of the accretion luminosity in these Seyfert AGN.

The average HSR SED of the type 2 and of the type 1 nuclei analysed in this work, and presented in Fig. 4, can be retrieved from http://www.iac.es/project/parsec/main/seyfert-SED-template.

ACKNOWLEDGMENTS

This work was initiated and largely completed during the stay of K. Tristram, N. Neumayer and A. Prieto at the Max-Planck Institut fuer Astronomie in Heidelberg.

REFERENCES

Alberdi A., Colina L., Torrelles J. M., Panagia N., Wilson A. S., Garrington S. I., 2006, ApJ, 638, 938
Beckert Th., Duschl W., 1997, A&A, 328, 95
Beckert T., Driebe T., Hoening S. F., Weigelt G., 2008, A&A, 486, L17
Beckmann V., Gehrels N., Shrader C. R., Soldi S., 2006, ApJ, 638, 642
Bland-Hawthorn J., Gallimore J. F., Tacconi L. J., Brinks E., Baum S. A., Antonucci R. R. J., Cecil G. N., 1997, Ap&SS, 248, 9
Bock J. J. et al., 2000, AJ, 120, 2904
Bohlin R. C., Savage B. D., Drake J. F., 1978, ApJ, 224, 132
Bond I. A. et al., 1996, A&A, 307, 708
Bruzual G., Charlot S., 2003, MNRAS, 344, 1000
Buchanan C., Gallimore J. F., O'Dea C. P., Baum S. A., Axon D. J., Robinson A., Elitzur M., Elvis M., 2006, AJ, 132, 401
Cardamone C., Moran E., Kay L., 2007, AJ, 134, 1263
Chiaberge M., Capetti A., Celotti A., 2001, MNRAS, 324, L33
Contini M., Prieto M. A., Viegas S. M., 1998, ApJ, 505, 621
Cotton W. D., Jaffe W., Perrin G., Woillez J., 2008, A&A, 477, 517
Dale D. A. et al., 2007, ApJ, 655, 863
de Grijp M. H. K., Lub J., Miley G. K., 1987, A&AS, 70, 95
Dewangan G. C., Griffiths R. E., 2005, ApJ, 625, L31
Dunne L., Eales S., Edmunds M., Ivison R., Alexander P., Clements D. L., 2000, MNRAS, 315, 115
Edelson R., Malkan A., 1986, ApJ, 308, 59
Edelson R., Malkan A., 1987, ApJ, 323, 516
Elmouttie M., Haynes R. F., Jones K. L., Sadler E. M., Ehle M., 1998, MNRAS, 297, 1202
Elitzur M., Shlosman I., 2006, ApJ, 648, L101
Elvis M. et al., 1994, ApJS, 95, 1
Evans I. N., Koratkar A. P., 2004, ApJS, 150, 73
Evans D. A., Kraft R. P., Worrall D. M., Hardcastle M. J., Jones C., Forman W. R., Murray S. S., 2004, ApJ, 612, 786
Fabbiano G., Kim D., Trinchieri G., 1992, ApJS, 80, 531
Ferrarese L., Mould J. R., Stetson P. B., Tonry J. L., Blakeslee J. P., Ajhar E. A., 2007, ApJ, 654, 186
Freeman K. C., Karlsson B., Lynga G., Burrell J. F., van Woerden H., Goss W. M., Mebold U., 1977, A&A, 55, 445
Gabel J. et al., 2003, ApJ, 583, 178
Gallimore J. F., Baum S. A., O'Dea C. P., 1996, ApJ, 458, 136
Gallimore J. F., Baum S. A., O'Dea C. P., 2004, ApJ, 613, 794
Gaskell C. M., Goosmann R. W., Antonucci R. R. J., Whysong D. H., 2004, ApJ, 616, 147
Genzel R. et al., 1998, ApJ, 498, 579
Glass I. S., 2004, MNRAS, 350, 1049
Greve A. et al., 2002, A&A, 390, L19
Haas M. et al., 2003, A&A, 402, 87
Haering-Neumayer N., Cappellari M., Rix H.-W., Hartung M., Prieto M. A., Meisenheimer K., Lenzen R., 2006, ApJ, 643, 226
Hao et al., 2005, ApJ, 625, L75
Hildebrand R., Whitcomb S., Winston R., Stiening R., Harper D., Mosely S., 1977, ApJ, 216, 698
Hoenig S., Beckert T., 2007, MNRAS, 380, 1172
Hoenig S., Prieto M. A., Beckert Th., 2008, A&A, 485, 33
Hummel H., van der Hulst J. M., Keel W. C., 1987, A&A, 172, 32
Jaffe W. et al., 2004, Nat, 429, 47
Kellermann K. I., Vermeulen R. C., Zensus J. A., Cohen M. H., 1998, AJ, 115, 1295
Kishimoto M., Hoenig S. F., Tristram K. R. W., Weigelt G., 2009, A&A, 493, 57
Krips M., Eckart M., Neri R., Schoedel R., Leon S., Downes D., Garcia-Burillo S., Combes F., 2006, A&A, 446, 113
Lal D. V., Shastri P., Gabuzda D. C., 2004, A&A, 425, 99
Landi R., Malizia A., Bassani L., 2005, A&A, 441, 69
Leeuw L. L., Hawarden T. G., Matthews H. E., Robson E. I., Eckart A., 2002, ApJ, 565, 131
Lichti G. G. et al., 1995, A&A, 298, 711
Lobanov A. P. et al., 2000, A&A, 364, 391
Lonsdale C. J., Doeleman S. S., Phillips R. B., 1998, AJ, 116, 8
McAlary C. W., McLaren R. A., McGonegal R. J., Maza J., 1983, ApJS, 52, 341
Malkan M., Gorjiam V., Tam R., 1998, ApJS, 117, 25
Marconi A., Schreier E. J., Koekemoer A., Capetti A., Axon D., Macchetto D., Caon N., 2000, ApJ, 528, 276
Marscher A., Jorstad S., Mattox J., Wehrle A., 2002, ApJ, 577, 85
Matt G. et al., 1997, A&A, 325, L13
Meisenheimer K. et al., 2007, A&A, 471, 453
Middelberg E. et al., 2004, A&A, 417, 925
Morganti R., Oosterloo T., Tadhunter C. N., Aiudi R., Jones P., Villar-Martin M., 1999, A&AS, 140, 355
Moshir M. et al., 1990, BAAS, 22, 1325
Munoz-Marin V. M., Gonzalez Delgado R. M., Schmitt H. R., Cid Fernandes R., Perez E., Storchi-Bergmann T., Heckman T., Leitherer C., 2007, AJ, 134, 648
Netzer H. et al., 2003, ApJ, 599, 933
Orienti M., Prieto M. A., 2009, MNRAS, in press (arXiv:0911.0852)
Perez-Olea D., Colina L., 1996, ApJ, 468, 191
Polletta M. et al., 2007, ApJ, 663, 81
Prieto M. A., Reunanen J., Kotilainen J., 2002, ApJ, 571, L7
Prieto M. A. et al., 2004, ApJ, 614, 135
Prieto M. A., Maciejewski W., Reunanen J., 2005, AJ, 130, 1472

Prieto M. A., Reunanen J., Beckert T., Tristram K., Neumayer N., Fernandez J. A., Acosta J., 2007, in Ho L. C., Wang J.-M., eds, ASP Conf. Ser. Vol. 373, The Central Engine of Active Galactic Nuclei. Astron. Soc. Pac., San Francisco, p. 600
Raban D., Jaffe W., Roettgering H., Meisenheimer K., Tristram K. R. W., 2009, MNRAS, 394, 1325
Reunanen J., Prieto M. A., Siebenmorgen R., 2009, MNRAS, in press (arXiv:0911.2112)
Rieke G. H., Lebofsky M., 1985, ApJ, 288, 618
Rouan D. et al., 2004, A&A, 417, L1
Rothschild R. E. et al., 2006, ApJ, 641, 801
Rowan-Robinson M. et al., 2005, ApJ, 129, 1183
Roy A. L., Norris R. P., Kesteven M. J., Troup E. R., Reynolds J. E., 1994, ApJ, 432, 496
Roy A. L., Norris R., Kesteven M., Troup E., Reynolds J., 1998, MNRAS, 301, 1019
Sadler E. M., Slee O. B., Reynolds J. E., Roy A. L., 1995, MNRAS, 276, 1373
Sandage A., Bedke J., 1994, The Carnegie Atlas Of Galaxies, Vol. I. Carnegie Inst. of Washington, Washington D.C.
Sanders D., Mirabel F., 1996, ARA&A, 34, 749
Sanders D. B., Soifer B. T., Elias J. H., Madore B. F., Matthews K., Neugebauer G., 1988, ApJ, 325, 74
Sanders D. B., Phinney E. S., Neugebauer G., Soifer B. T., Matthews K., 1989, ApJ, 347, 29
Sanders D. B., Mazzarella J. M., Kim D.-C., Surace J. A., Soifer B. T., 2003, AJ, 126, 1607
Sanders D. B. et al., 2007, ApJS, 172, 86
Sazonov S., Revnivtsev M., Krivonos R., Churazov E., Sunyaev R., 2007, A&A, 462, 57
Schmitt H. R., Ulvestad J. S., Antonucci R. R. J., Kinney A. L., 2001, ApJS, 132, 199
Schonfelder V. et al., 2000, A&AS, 143, 145
Scott J. E. et al., 2005, ApJ, 634, 193
Shen Z.-Q. et al., 1998, AJ, 115, 1357
Shinozaki K., Miyaji T., Ishisaki Y., Ueda Y., Ogasaka Y., 2006, AJ, 131, 2843
Siebenmorgen R., Krugel E., Spoon H. W., 2004, A&A, 414, 123
Soldi S. et al., 2005, A&A, 444, 431
Sopp H. M., Alexander P., 1991, MNRAS, 251, 14P
Steinle H. et al., 1998, A&A, 330, 97
Stickel M., Lemke D., Klaas U., Krause O., Egner S., 2004, A&A, 442, 39
Terashima Y., Iyomoto N., Ho L. C., Ptak A. F., 2002, ApJS, 139, 1
Thean A., Pedlar A., Kukula M. J., Baum S. A., O'Dea C. P., 2000, MNRAS, 314, 573
Tingay S. J., Murphy D. W., 2001, ApJ, 546, 210
Tingay S. J., Preston R. A., Jauncey D. L., 2001, AJ 122, 1697
Tomono D., Doi Y., Usuda T., Nishimura T., 2001, ApJ, 557, 637
Tristram K. R. W. et al., 2007, A&A, 478, 837
Tristram K. R. W. et al., 2009, A&A, 502, 67
Tully R. B., 1988, Nearby Galaxy Catalog. Cambridge Univ. Press, Cambridge
Turler M. et al., 1999, A&AS, 134, 89
Turner T. J., Pounds K. A., 1989, MNRAS, 240, 833
Turner T. J., Perola G. C., Fiore F., Matt G., George I. M., Piro L., Bassoni L., 2000, ApJ, 531, 245
Ulvestad J. S., Wilson A. S., 1984, ApJ, 285, 439
Unger S. W., Lawrence A., Wilson A. S., Elvis M., Wright A. E., 1987, MNRAS, 228, 521
Vasudevan R. V., Fabian A. C., 2007, MNRAS, 381, 1235
Ward M., Elvis M., Fabbiano G., Carleton N. P., Willner S., Lawrence A., 1987, ApJ, 315, 74
Weedman D. W. et al., 2005, ApJ, 633, 706
Weigelt G., Wittkowski M., Balega Y. Y., Beckert T., Duschl W. J., Hofmann K.-H., Men'shchikov A. B., Schertl D., 2004, A&A, 425, 77
Whysong D., Antonucci R., 2004, ApJ, 602, 116
Witt A., Thronson H., Capuano J., 1992, ApJ, 393, 611
Yang M., Phillips T., 2007, ApJ, 662, 284
Yaqoob T., Reeves J. N., Markowitz A., Serlemitsos P. J., Padmanabhan P., 2005, ApJ, 627, 156
Young A. J., Wilson A. S., Shopbell P. L., 2001, ApJ, 556, 6
Zdziarski A. A., Poutanen J., Johnson W. N., 2000, ApJ, 542, 703

This paper has been typeset from a TEX/LATEX file prepared by the author.